Aseismic Motions Drive a Sparse Seismicity During Fluid Injections Into a Fractured Zone in a Carbonate Reservoir

Laure Duboeuf

Louis De Barros

Frédéric Cappa

Yves Guglielmi

Anne Deschamps

Simon Seguy

Abstract

An increase in fluid pressure in faults can trigger seismicity and large aseismic motions. Understanding how fluid and faults interact is an essential goal for seismic hazard and reservoir monitoring, but this key relation remains unclear. We developed an in situ experiment of fluid injections at a 10 meter scale. Water was injected at high pressure in different geological structures inside a fault damaged zone, in limestone at 280 m depth in the Low Noise Underground Laboratory (France). Induced seismicity, as well as strains, pressure, and flow rate, was continuously monitored during the injections. Although nonreversible deformations related to fracture reactivations were observed for all injections, only a few tests generated seismicity. Events are characterized by a 0.5-to-4 kHz content and a small magnitude (approximately −3.5). They are located within 1.5 m accuracy between 1 and 12 m from the injections. Comparing strain measurements and seismicity shows that more than 96% of the deformation is aseismic. The seismic moment is also small compared to the one expected from the injected volume. Moreover, a dual seismic behavior is observed as (1) the spatiotemporal distribution of some cluster of events is clearly independent from the fluid diffusion (2) while a diffusion-type pattern can be observed for some others clusters. The seismicity might therefore appear as an indirect effect to the fluid pressure, driven by aseismic motion and related stress perturbation transferred through failure.

1 Introduction

The seismicity associated with deep fluid injections within geological reservoirs has become an important concern related to the developments of subsurface energy extraction and storage (Bachmann et al., 2012; Bao &

Eaton, 2016; Cornet, 2012; Cornet et al., 1997; Ellsworth, 2013; Elsworth, Spiers, & Niemeijer, 2016; McGarr, 2014). For instance, the enhanced geothermal system at Soultz-sous-Forêts, France (Cuenot, Dorbath, & Dorbath, 2008; Schmittbuhl et al., 2014), or in Geysers, USA (Trugman et al., 2016), shows a clear and intense seismicity temporally synchronized with injection periods. Other examples show that fracking operations and wastewater disposals in the central U.S. induced a sharp increase of the seismicity rates since the early 2000 (Ellsworth et al., 2015; Keranen et al., 2014; McGarr et al., 2015; McNamara et al., 2015; Walsh & Zoback, 2015). This type of seismicity is generally of small moment magnitude ($M_w < 3$). However, some of these injection-induced earthquakes have reached magnitudes greater than 5 (Ellsworth, 2013; Keranen et al., 2014; Petersen et al., 2016; Weingarten et al., 2015), such as the 2011 M_w 5.6 Prague (Barnhart et al., 2014; Keranen et al., 2013; Norbeck & Horne, 2016; Sumy et al., 2017; Sun & Hartzell, 2014) or the September 2016 M_w 5.8 Pawnee (Walter et al., 2017; Yeck et al., 2017) earthquakes in Oklahoma, USA.

Furthermore, pervasive fluids into the upper brittle crust can also trigger natural seismicity. Sometimes, fluid pressure perturbations can help to trigger large earthquakes, such as the M_w 7.7 2001 Buhj earthquake (Kayal et al., 2002), which was located in a fluid-filled area identified through high Poisson's ratio. Fluids are also suspected to be a driving factor for seismic swarms (Cappa, Rutqvist, & Yamamoto, 2009; Hainzl, 2004; Hainzl et al., 2006; Leclère et al., 2012; Shelly et al., 2015). For example, seismic swarms observed in the Gulf of Corinth (Greece) are related to the diffusion of fluid overpressures (Duverger et al., 2015; Pacchiani & Lyon-Caen, 2010). Moreover, observations indicated that even strong rainfalls can be a driver of seismicity (Hainzl et al., 2006; Miller, 2008; Rigo et al., 2008).

At the same time, fluids may induce deformation without triggering seismicity. Aseismic motion, i.e., slow rupture that does not produce seismic waves, is now admitted to be an important process during fluid injections in geological reservoirs (Cornet, 2012, 2016; Zoback et al., 2012). For instance, clear observations of aseismic slip have been identified at geothermal sites like Soultz-sous-Forêts, France (Calò et al., 2011; Cornet et al., 1997; Lengliné et al., 2017), where an important part of the deformation was aseismic even if intense seismicity occurred. The same pattern was observed in the Mayet de la Montagne experiments (Scotti & Cornet, 1994) where water injections in a 800 m long borehole mainly drove aseismic deformation. Aseismic motion was also observed in controlled in situ fluid injection experiments at meter scale in limestone (Guglielmi et al., 2015) or in shale (De Barros et al., 2016). At the laboratory scale, Goodfellow et al. (2015) performed fluid injection experiments on granite samples under triaxial stresses and showed that most of the deformation is aseismic during the fluid pressurization.

However, despite these clear evidences, the triggering and driving mechanisms of seismicity and aseismic motions by the fluid pressure remain

unclear, mainly because they are controlled by complex interactions of frictional and fluid flow properties and behaviors together with the evolving state of stress during fluid injections. The classical concept assumes that an increase in fluid pressure reduces the effective stress normal to fault and its resistance, leading up to seismicity (Healy et al., 1968; Hubbert & Rubey, 1959; Parotidis et al., 2003; Shapiro et al., 2002). In this model, the seismicity distribution is therefore controlled by the magnitude and diffusion of the fluid pressure. Other processes triggering seismicity can be fracture propagation through hydrofracturing (Cornet, 2000) and poroelastic stress perturbation transferred through failure away from a pressure source (Goebel et al., 2017). Nevertheless, recent observations (De Barros et al., 2016; Guglielmi et al., 2015; Zoback et al., 2012) showed that fluid pressure first drives an aseismic fault rupture. The seismicity appears as a secondary process and a response of the surrounding medium to the aseismic rupture. This complex behavior was successfully explained at field scale by a transition from stable to unstable slip using a slip rate dependency of fault friction (Guglielmi et al., 2015; Ruina, 1983).

Although the previous observations provide key insights into how fluid pressures can trigger seismicity or aseismic deformation, the links between fluid pressure diffusion, aseismic motions, and seismicity are poorly constrained. Hence, more accurate observations of seismicity, deformation, and fluid pressure near and within faults are required in order to improve understanding of these interconnected mechanisms and to bridge the gap between small-scale (cm) laboratory experiments and large-scale (km) observations. To this aim, controlled fluid injection experiments at a meter to tens of meters have already been developed in limestones by Guglielmi et al. (2015) and Derode et al. (2015) as well as in shales (De Barros et al., 2016; Rivet et al., 2016). Here we have performed a series of fluid injection experiments with a proximal (meters) array of 31 high-sensitivity seismic sensors within the damage zone of the same fault zone previously tested in Guglielmi et al. (2015), but with a limited seismic network (only three sensors). The aim of the present study is to activate different parts of the fault damage zone by injecting high fluid pressure directly in existing geological structures (faults, fractures, and bedding planes) and to monitor both the hydromechanical and seismological responses. In this paper, we mainly focus on the analysis of the seismological data that we interpret in the light of detailed geological and hydromechanical contexts. First, we present the geology of the tested fault zone and the experimental setting of our experiments. We then describe the monitoring system, and the processing methods are presented. During the injections, location, magnitude, and source parameters are first deduced from the observed seismic events. We then compare the amount of seismic motion to the amount of aseismic deformation measured at the injection with the Step-Rate Injection Method for Fractures In-situ Properties (SIMFIP) borehole displacement sensor (Guglielmi et al., 2013). Finally, we discuss the different

seismic behaviors, potential mechanisms, and the reasons why the seismicity appears as an indirect effect of fluid injections that mainly generate large aseismic motions.

2 Geological and Experimental Settings

2.1 Geology and Properties of the Tested Fault Zone

The experiments took place at 280 m depth within the Low Noise Underground Laboratory (LSBB, http://lsbb-new.prod.lamp.cnrs.fr) located in the southeast of France sedimentary basin (Figure 1a). Four kilometers of subhorizontal galleries allow a direct access to an unaltered fractured cretaceous limestone made up of platform carbonates facies and considered as an analogue to the deep Middle East carbonate reservoir fields (Figure 1b) (Jeanne, Guglielmi, Lamarche, et al., 2012). Five 20 m long vertical cored holes were drilled from the gallery floor (Figure 1b) to collect rock samples and to place sensors. Two of these wells (B2 and B3; Figures 1c and 2), 20.85 m and 21.25 m deep, respectively, were used to perform the fluid injections.

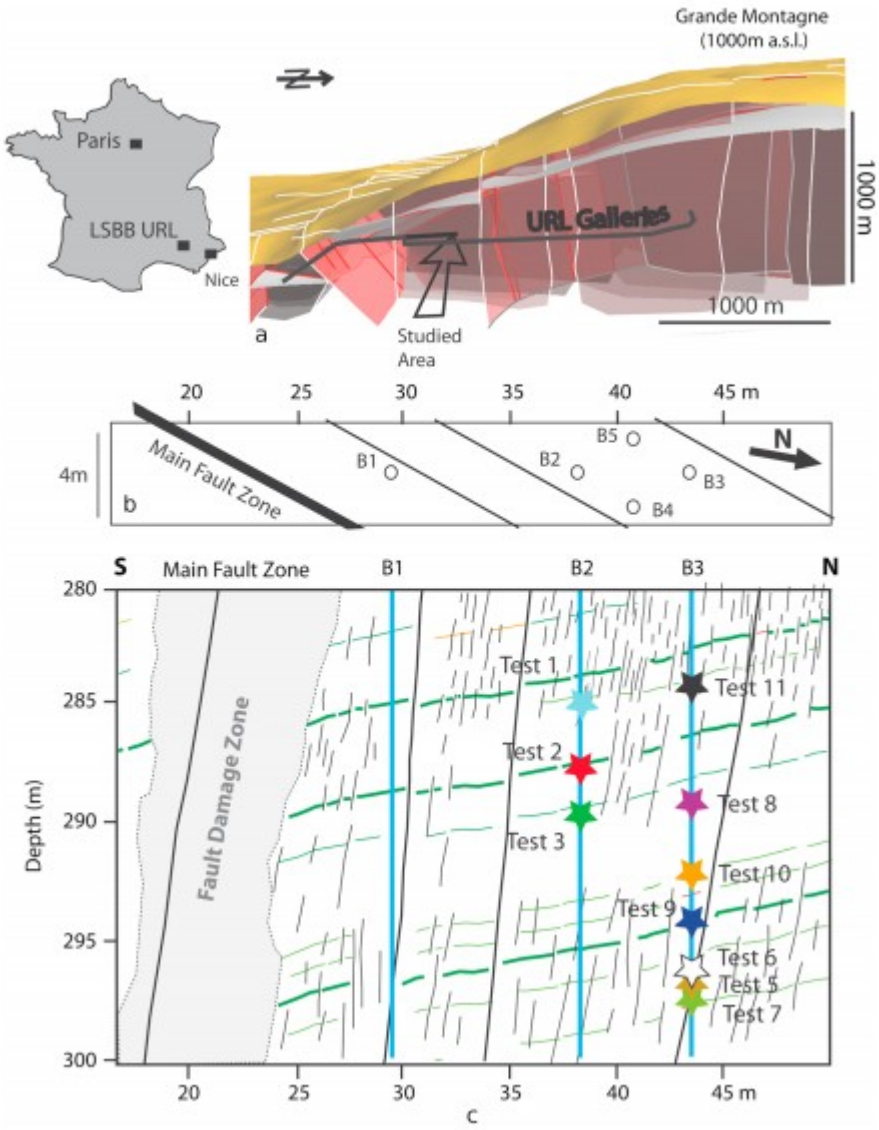

Figure 1

Regional geological setting. (a) Three-dimensional geological model of the LSBB and location of the gallery experiment. (b) Horizontal and (c) vertical views of the gallery. On the horizontal view, main fault and secondary faults are represented as well as the five boreholes. The injection wells are B2 and B3. On the vertical view, the stars represent the 10 injection intervals.

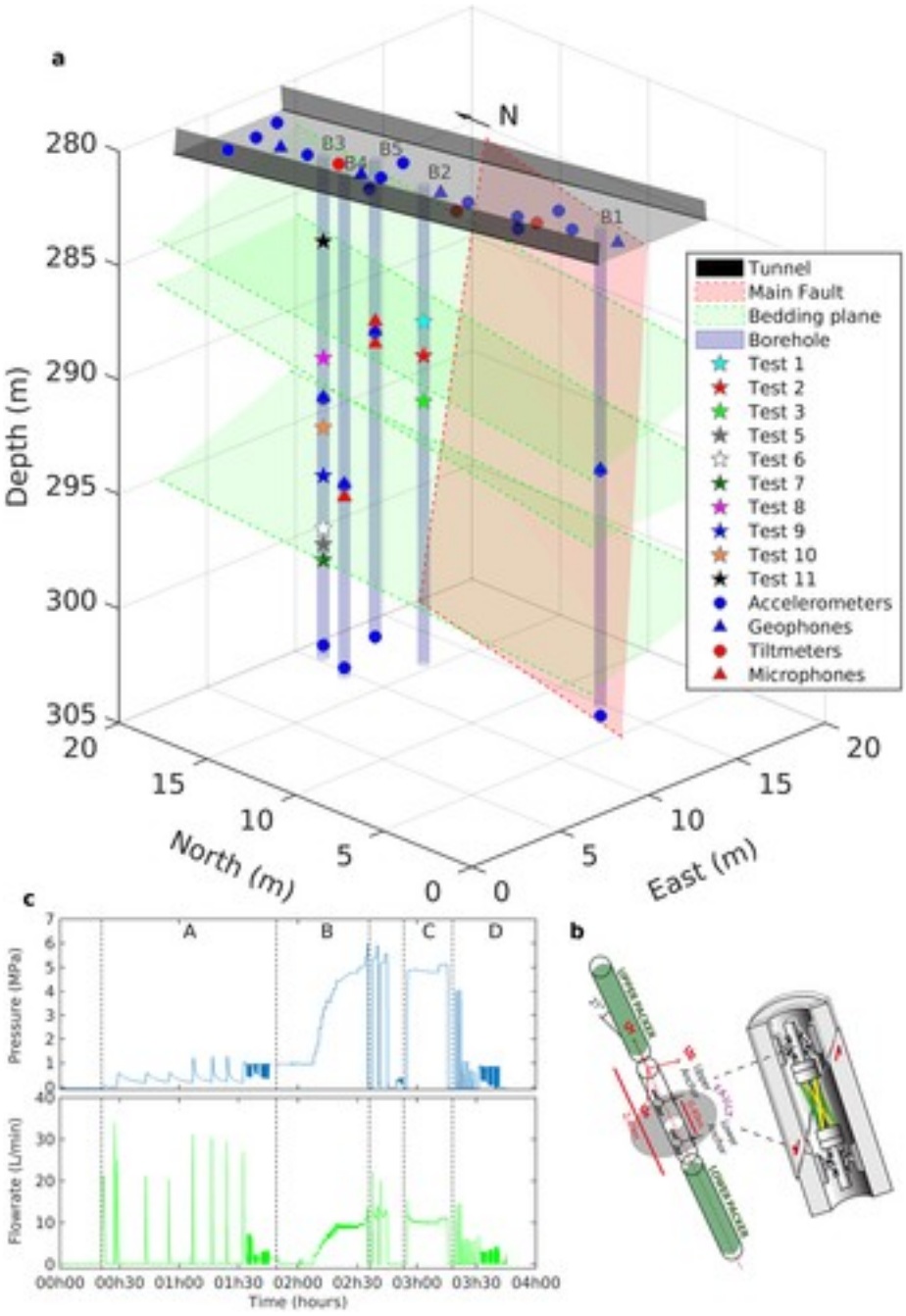

Figure 2

(a) Instrumented fault zone, geological setting, and monitoring instruments—The main fault is represented by a red plane. The main bedding planes are represented by the green planes. The floor of the gallery is represented by the grey area and the five vertical boreholes by the blue cylinders. Seismic instruments are in blue, circles for accelerometers, and triangles for geophones. The red triangles show the microphones, and the red circles show the tiltmeters. The stars represent the injection test locations, which are performed thanks to the (b) probe SIMFIP. (c) A typical injection test-fluid pressure (blue curve) and flow rate (green curve) versus time. Four different steps: (A) small pulses in the elastic domain before rupture to evaluate the permeability, (B) increase of the pressure step-by-step, (C) maintenance of a quasi-constant pressure period, and (D) pulses to evaluate the permeability after rupture.

The limestones display ≲1 to 5 meter thick layers. They are affected by a kilometric normal fault, oriented N030°-85, and by three secondary faults all belonging to the same fault system, respectively, located at 20, 30, 35, and 45 m on the gallery floor level in Figure 1c. The main fault is connected to a 20 m thick fracture zone, including subvertical, subparallel fractures of 1 to 10 m length (Jeanne, Guglielmi, & Cappa, 2012). The fracture density progressively decreases away from the fault core. The experiments were performed in a 40 m × 20 m × 20 m volume of this fractured zone, which mainly contains N10° to N30° and ~70° dipping east or west fractures and secondary faults, N090°–20° to 50°S fractures, and N110°-to-135°-20-to-35°SW bedding planes.

Close to the main fault, there is an ~5 m thick and highly fractured-to-crushed fault damage zone that is affecting all the layers. Smaller damage zones of a few centimeters to 1 meter in thickness are observed around the secondary faults (Figure 1 zone represented in grey). In the zone of experiments, which is ~18 m away from the main fault, there is a 5 m thick low fractured layer at 290-to-295 m depth, intercalated between an upper and a deeper highly fractured one. This “layering” in the fracturation was interpreted as differences in the damage of the sedimentary layer during faulting (Figure 1c). This results in a strong heterogeneity in the rock quality and hydraulic properties that will be discussed later in the paper (for details see Jeanne, Guglielmi, Lamarche, et al., 2012).

The site of experiments is located in the unsaturated zone of the reservoir. The state of stress has been computed by Guglielmi et al. (2015) using a forward fully coupled numerical analysis of the injection tests of a first experiment and refined using the new data from the present hydraulic tests on preexisting fractures. The high fracture density of the experiment zone (Jeanne, Guglielmi, & Cappa, 2012) and the wide range of fracture initial permeability (see section 4.1) strongly control the local state of stress and condition the protocol to estimate stresses. Optical logging of the wells after the tests did not show any induced fractures, proving that tests only trigger reactivation of natural preexisting fractures. Shut-in pressures were difficult to identify because complete closure of the preexisting fractures never occurred. We applied the fracture reopening protocol prescribed in Haimson and Cornet (2003), and we used the nonreversible displacements measured with the SIMFIP probe (see section 2.2 and Figure 2) to extract both the reopening pressure and the slip vector on the reactivated planes and inverse the stresses using all the tests (except test 10 where no fracture was identified). From this protocol, the maximum principal stress $\sigma_1 = 6 \pm 0.4$ MPa is subvertical and dips 80°S ± 5°, $\sigma_2 = 5 \pm 0.5$ MPa is subhorizontal and oriented N20° ± 20°, and $\sigma_3 = 3 \pm 1$ MPa is subhorizontal and oriented N110° ± 20°. Stress estimation, however, is beyond the scope of this paper.

2.2 Instrumental Device and Injection Protocol

A hydromechanical probe was used to perform the injections in the B2 and B3 boreholes (Figures 2a and 2b), following the Step-Rate Injection Method for Fractures In-situ Properties (SIMFIP) (Guglielmi et al., 2013). This probe allows capturing the coupled hydromechanical response of borehole intervals straddling different fractured carbonate facies. A 2.4 m injection chamber is isolated in the borehole between two inflatable packers that hold the probe at the convenient depth. In the injection chamber where the fractures of the fault zone are present, changes in fluid pressure, fractures mechanical displacements, and temperature were simultaneously monitored with a respective accuracy of 0.1 kPa, 3 µm, and 0.1°C. Three other pressure and temperature sensors are located outside the chamber to monitor the injection variations, whereas the flow rate is directly measured at the fluid injection pump.

The fault displacements are measured with a three-dimensional extensometer that is composed of two undeformable rings anchored above and below the tested fractures in the borehole. These two rings are connected by an array of six deformable tubes instrumented with fiber optic Bragg strain gauges. Once the sensor is anchored, it is completely independent from the straddled system of the probe. Thus, a fracture movement eventually caused by the chamber pressurization will produce a relative displacement between the upper and the lower (considered fixed) anchors inducing deformations of the tubes. An algorithm allows to inverse the tube strains into the relative three-dimensional displacement of one fault compartment toward the other one (Guglielmi et al., 2013).

Within the framework of this study, we performed 10 high-pressure fluid injection tests at different depths and in different interval geologies (Figures 1c and 2a). As shown in Figure 2c, a typical test (Test 9, see location in Figure 1) is characterized by a minimum of four major cycles, respectively, low-pressure pulse tests, repeated high-pressure step-rate tests to activate the fault, and final low-pressure pulse tests. Low-pressure pulse injections are conducted in order to evaluate the initial and post-test permeability of the medium. In Figures 3a and 3b, we present an example of the injected flow rate-versus-pressure and of the displacement-versus-pressure variations measured parallel and normal to a N145E-26°W activated fracture during the first pressure step-rate test (STR1 in Figure 2a). Results show that there is a linear flow rate-versus-pressure increase until a pressure of 4.06 MPa is reached, then there is a flow rate step increase followed by a nonlinear variation from 4.06 to 5.35 MPa (Figure 3a). All mechanical displacement curves show a variation tangential and normal to the activated fracture plane, and a residual displacement at the end of the cycle when pressure is set back to its initial value (0 MPa) (Figure 3b). Up to 3.8 MPa, there is a linear relationship between displacements and pressure increase. Using the low-pressure cycles conducted during the test, it can be demonstrated that below a pressure of 3.8 MPa, the repeatability of the signals and the null residual displacement highlight the poroelastic response of the fracture.

Above a pressure of 3.8 MPa, all displacements strongly deviate from linearity. A fracture normal displacement associated to shearing initiates synchronously to the step increase in flow rate variations, highlighting a fracture hydraulic conductivity increase. Then, above a pressure of 5.1 MPa, there is a fracture normal closing while shearing and flow rate increase. During this high-pressure period, the fracture's hydraulic conductivity is increasing exponentially with shear. Fracture normal closing can be interpreted as either compaction induced by shear or as elastic closing because the injected flow rate is not high enough to maintain the pressure-induced opening. The amount of fracture's movements monitored above a pressure of 3.8 MPa corresponds to the residual displacements at the end of the test. In Figure 4, the periods with pressure greater than 5.1 MPa correspond to a mainly inverse slip on the N15E-26°W activated plane (red segment in Test 9 graph). Movements above a pressure of 3.8 MPa are interpreted as nonreversible fracture's displacements that are associated to seismic events (Figures 5 and 6).

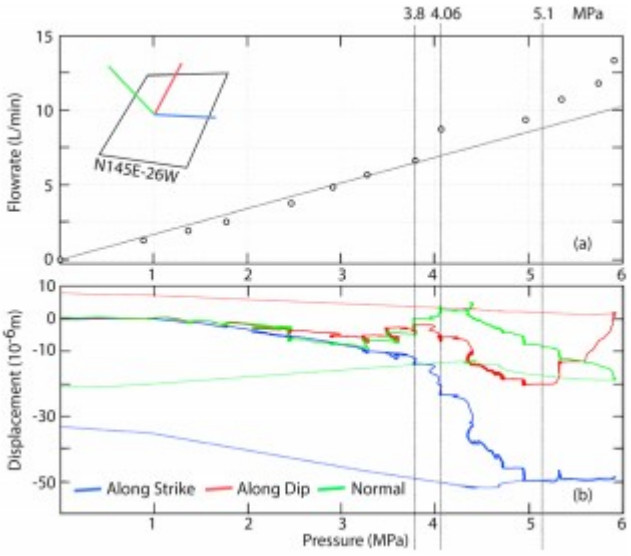

Figure 3

Typical fluid pressure-versus-displacement response monitored during Test 9 cycle B with the SIMFIP instrument (the continuous lines show the pressure step up period; the dashed lines show the pressure step down period). (a) Injected flow rate versus pressure (points are picked at each constant pressure step); (b) displacement tangential and normal to the activated fracture plane.

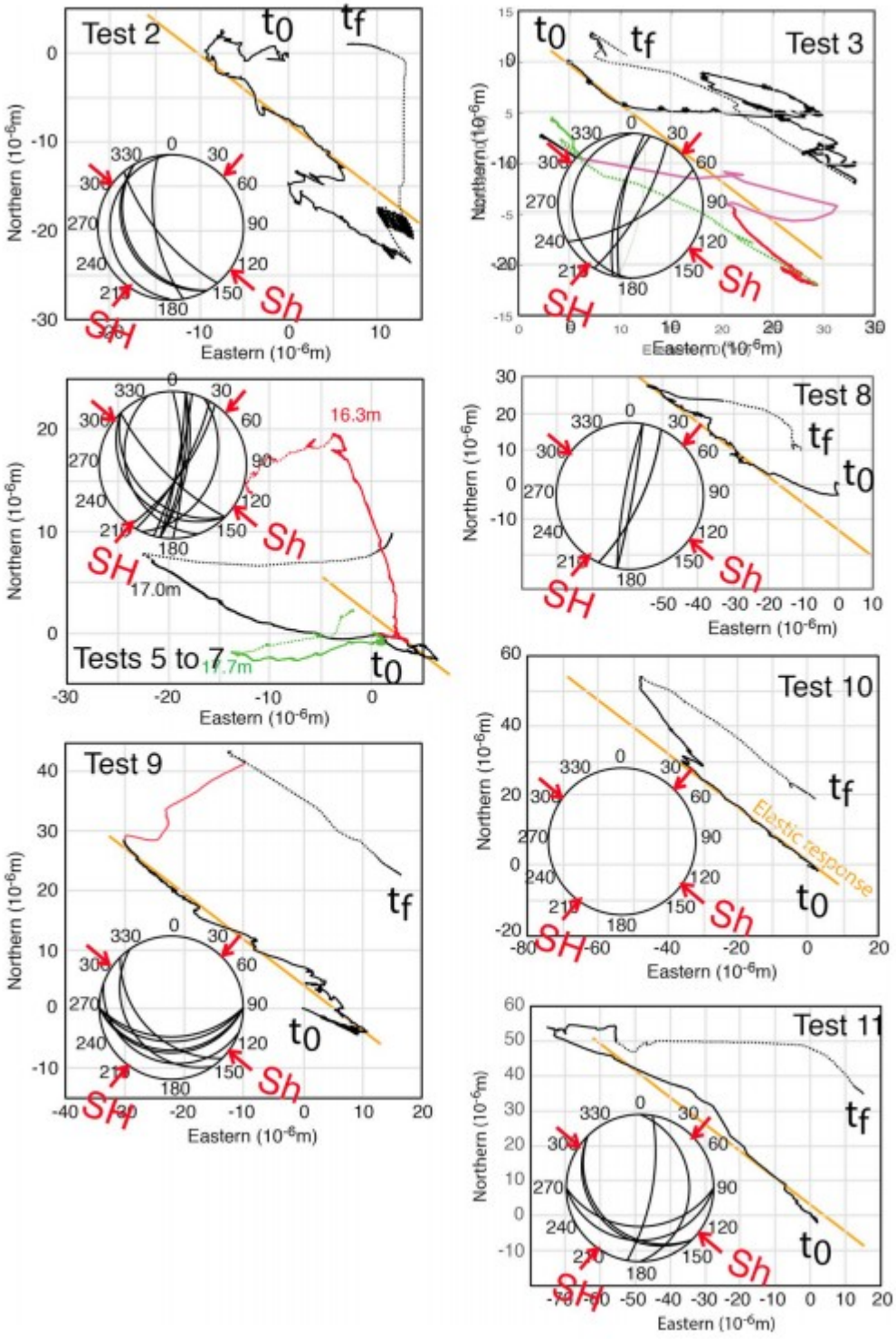

Figure 4

Borehole wall displacements during injections for each test where t_0 is the injection start and t_f is the injection end; continuous line figures the step-up pressure and discontinuous line the step-down pressures.

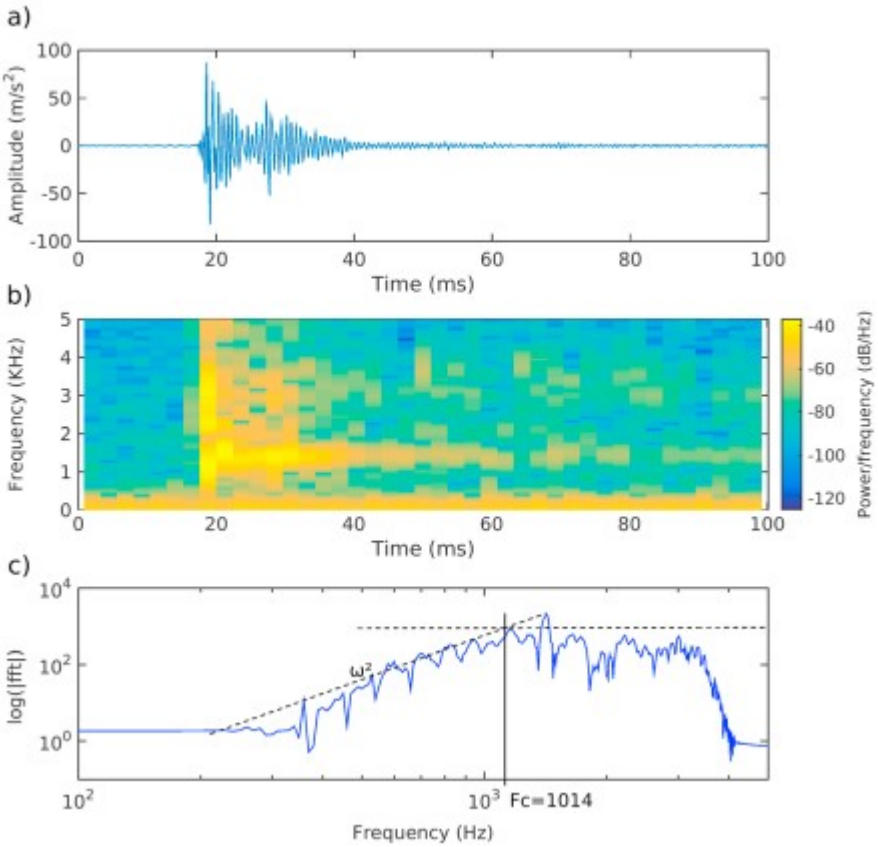

Figure 5

Example of a filtered seismic event and its frequency content. (a) Acceleration filtered between 600 and 3,000 Hz, (b) corresponding seismogram, and (c) Fourier spectrum, with a sketch of the fitting model used for the spectral analysis.

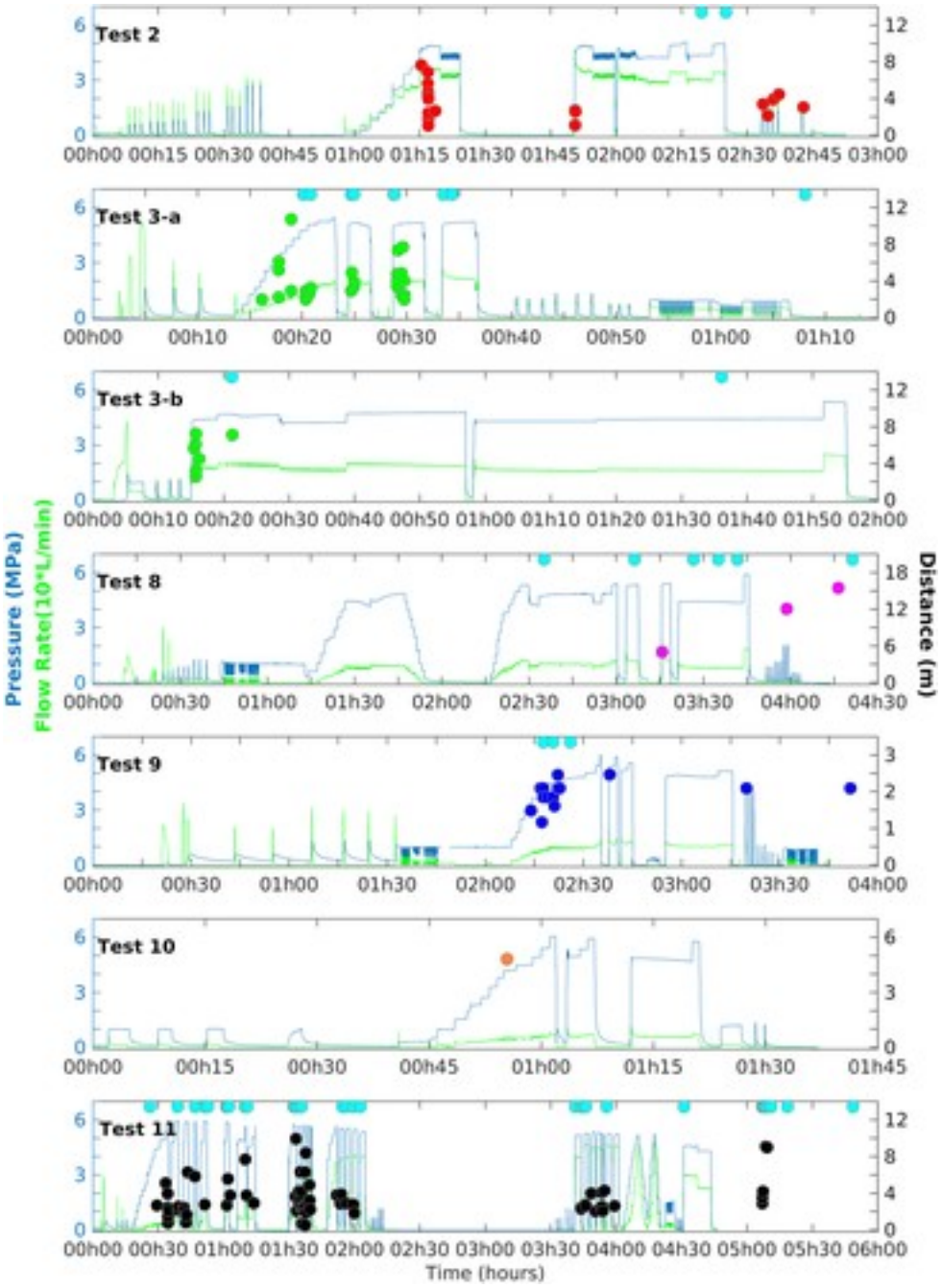

Figure 6

Pressure (blue line), flow rate (green line), and distance of seismic events (colored dots: red for Test 2, green for Test 3, pink for Test 8, blue for Test 9, orange for Test 10, and black for Test 11) to the injection point versus time for Test 2, Test 3-a, Test 3-b, Test 8, Test 9, Test 10, and Test 11. The light blue dots represent detected but not located events.

A complete hydromechanical analysis of all the tests is beyond the scope of this paper. In the following analysis, we will use the residual displacement vector orientation and magnitude as a proxy to estimate the activated fracture slip in each interval test and to compare with dynamic ruptures inferred from induced earthquake source characteristics. The residual

displacement is the displacement value after the pressure in the interval has returned to initial (vector in Figure 4).

The first four fluid injections took place in borehole B2 (Figure 2a) at depths of 6, 7.5, 9.5, and 17.8 m, respectively (depths correspond to the middle of the straddle interval). The following tests (5 to 11) were performed in borehole B3 at 17, 16.3, 17.7, 8.85, 14, 11.9, and 3.75 m depths, respectively (see Table S1 in the supporting information). These tests allowed to investigate the hydromechanical and seismic responses of the following geological structures inside the injection chamber: (1) subparallel bedding planes mostly oriented N135 ± 10°-25 ± 5°SW (Tests 1, 2, 9, and 11) and (2) different types of fractures, preferentially oriented N10 ± 10°-75 ± 5°E and N10 ± 10°-75 ± 5°W (Tests 3, 5, 6, 7, 8, and 10). A bypass of the packers through rock fractures occurred during Test 1 with consequences on the injection chamber integrity. For this reason, Test 1 is not included in this study. Tests 5 to 7 are very close to each other and injection chambers strongly overlap. The idea was to explore more accurately an ~0.5 m thick fault zone intersecting the borehole B3.

During the experiments, the seismicity was monitored by a dense network of 50 sensors (Figure 2a) located both in the boreholes and on the gallery floor. The short distances (3 to 35 m) between the injection points and the sensors increase the network sensibility. Previous in situ experiments in similar conditions (De Barros et al., 2016; Derode et al., 2015) highlight the high-frequency contents (greater than 1 kHz) of such induced seismicity. Therefore, accelerometers with a broad and high-frequency response have been chosen as the network backbone. Eight triaxial accelerometers (PCB356B18, frequency from 2 Hz to 4 kHz) have been installed in the four boreholes surrounding the injection well. Four of the borehole accelerometers were set down to the boreholes bottom (i.e., 20 m depth below the gallery ground), while the other four sensors were anchored at 10.52, 10.52, 13.52, and 7.52 m depths, respectively (Figure 2a). Fourteen vertical BK4383 accelerometers completed the seismic network on the gallery floor with frequency ranges varying from 10 Hz to 10 kHz. In addition to the accelerometers, we also installed geophones, microphones, and tiltmeters. This sensor diversity allows to probe a large frequency range from static to 20 kHz. Seismic, mechanical, and hydrological data are continuously recorded, and the time is synchronized by an acquisition station (Gantner), with a sample rate of 1 kHz for the hydromechanical data and 10 kHz for the accelerometer data.

Calibration shots were performed in order to check the network responses and then to test our processing data methods. These shots consisted in weight drops in the injection boreholes and hammer shots on the wall and the floor of the gallery. The medium is composed of limestones which allow to consider it as homogeneous at the seismic wavelengths of several meters that we considered here. By using calibration shots, a mean *P*wave velocity of 4,750 m/s is estimated while the mean *S* wave velocity is about 2,750 m/s

(see Figure S1 in the supporting information). The ratio between P and S wave velocities is found to be equal to , a value consistent with Wilkens, Simmons, and Caruso (1984).

3 Methods

From the recorded continuous data, a semi-automatic seismic event detection based on waveform amplitude is used. When the energy is greater than a defined threshold on at least 10 sensors, a possible seismic event is suspected and extracted. Then, selected candidates were checked by eye screening and 215 earthquakes were kept from the full data set. As some of them visually present waveform similarities, events within each injection tests were cross-correlated. Families of similar events with a minimal cross-correlation coefficient greater than 0.7 will then be used for the location.

The location method is unusual as we performed in the same inversion absolute and relative locations. It is based on the minimization of a normalized cost function (equation 1), which is built to use simultaneously the P and S wave travel times (t_p and t_s), the P and S wave time differences ($t_p - t_s$), and the differential times between similar events. Consequently, this method takes advantage of using all available travel-time data. With this approach, the most accurate location is expected (Zecevic et al., 2016). The clear P and S wave arrival times (and) were manually picked for the full event set on each accelerometer. Then, if seismic events belong to the same cluster and have a similar waveform, we use the double-time difference principle (Shearer, 1997; Waldhauser & Ellsworth, 2000) and compute the differential travel-time between two stations for one seismic event (Zecevic et al., 2016). Afterward, we define weights on the pick quality W_p and W_s, the sensor locations W_c, the correlation computations W_{dd} , and the delay time between stations $W_{\mathrm{cA}}W_{\mathrm{cB}}$. Finally, we introduce weights to balance each part of the equation relatively to each other (A_s for the Swave, A_{sp} for the S-to-P differences, and A_{dd} for the double-difference times). The cost function is therefore given by

$$\begin{aligned}\mathrm{RMS} = {} & W_p W_c \sum_i \left[\overline{t_{p\,i}^{\mathrm{obs}}} - \overline{t_{p\,i}^{\mathrm{th}}}\right]^2 + A_s W_s W_c \sum_i \left[\overline{t_{s\,i}^{\mathrm{obs}}} - \overline{t_{s\,i}^{\mathrm{th}}}\right]^2 \\ & + A_{sp} W_p W_s W_c \sum_i \left[\left(t_{s\,i}^{\mathrm{obs}} - t_{p\,i}^{\mathrm{obs}}\right) - \left(t_{s\,i}^{\mathrm{th}} - t_{p\,i}^{\mathrm{th}}\right)\right]^2 + A_{\mathrm{dd}} W_{\mathrm{dd}} W_{\mathrm{cA}} W_{\mathrm{cB}} \sum_j \sum_i \left[\left(t_{\mathrm{dd}\,ij}^{\mathrm{cal}} - t_{\mathrm{dd}\,ij}^{\mathrm{th}}\right)\right]^2 \end{aligned} \quad (1)$$

where the subscripts “i” and “j” denote the sensors and the superscripts “th,” “calc,” and “obs” are, respectively, the theoretical, the computed, and the observed times.

The theoretical times used in equation 1 are computed for a grid of potential sources, with a step of 0.25 m in the three space directions. This value of 0.25 m was found as the best ratio between the computation time and the obtained location. The grid point, for which the RMS function is minimum, is kept as the most likely source. This method has been tested on the calibration shots, which enables us to adjust the weights and to select the

suitable data to use in the inversion. The *P* wave travel time and the double-difference times are always used for the location but the *S* phase is optionally used. Indeed, testing this method on the calibration shots highlights that wrong *S* phase can completely twist results. Consequently, *S*waves are only used when the location obtained with the *S* travel times is similar from the one computed without them. The location approach gives a maximum error of 0.50 m for the calibration shots.

As we made the assumption of a homogeneous medium, the sensibility of the method to a wrong velocity model is tested. We locate the calibration shots for *P* wave velocity varying between 4,400 and 5,100 m/s. The *S* wave velocity varies according to the *P* wave velocity with a constant ratio of . Whatever the used velocity, the inversion algorithm found the calibration shots with an error weaker than 1 m from the true location. Therefore, the velocity model has a limited influence on the event location accuracy as an error of 300 m/s on the velocity does not significantly change the calibration shot locations (see Figure S2 in the supporting information). Thus, tests on calibration shots underline that an accurate location is obtained for events inside the network.

Within this framework, a grid search algorithm is used and a contour (i.e., confidence envelop) surrounding the most probable event position can be defined as the maximum location error. For most of the seismic events, the 98% confidence interval is within an ellipsoid with large axis smaller than 3 m. Finally, this method allows to locate 137 seismic events (i.e., 64% of total amount of the data set) with error generally lower than 1.5 m. These events are found to occur within the sensor network.

Then, we investigate the corner frequencies and the moment magnitudes of these events through a spectral analysis. Fourier spectra (Figure 5) are computed using both the *P* and *S*phases because the time lag between both is often too small to clearly separate them. The spectrum is fitted by a ω^2 slope at low frequencies and by a flat plateau for the highest ones (Boore, 1983; Brune, 1970; Brune, Archuleta, & Hartzell, 1979). The attenuation coefficient influence on the corner frequency estimation was tested for several values ranging from 30 to 1,000. For each seismic event, the corner frequencies vary of less than 100 Hz with a mean value obtained for an attenuation coefficient close to 70. As the radiation pattern is unknown, the corner frequencies computed for every sensor are averaged and a mean radiation pattern coefficient of 0.52 (Aki & Richards, 1980) is assumed. The magnitude errors associated with this hypothesis are between −0.5 and +0.2 (Daniel, 2014; Von Seggern, 1970). Considering other assumptions, the use of both *P* and *S* phases in the spectral analysis, the number of stations used, or the velocity model (Stork, Verdon, & Kendall, 2014), the magnitude values might have an error up to 1 order of magnitude. However, the constant way of performing this analysis allows us to compare magnitudes among them.

Finally, we investigate the earthquake source size as well as the stress drop assuming a circular crack rupture (Eshelby, 1957). *P* and *S* waves are both used to compute the corner frequencies. However, as the *S* waves have larger amplitude, we assume that the wavefield is dominated by *S* waves. In this case, the radius of a seismic source (r) is expressed as follows:

$$r = k \times \frac{v_s}{f_c} \quad (2)$$

where v_s is the *S* wave velocity, f_c is the corner frequency, and k is a constant that depends on both rupture (type and velocity), slip velocities, geometry of the fault, and failure directivity (e.g., Kaneko & Shearer, 2014). For small earthquakes, the rupture velocity may vary from 0.4 to 0.9 of the *S* velocity (Imanishi et al., 2004). We used here two different values: $k = 0.21$ and $k = 0.12$, which correspond to a rupture velocity of 0.9 (Madariaga, 1977) and 0.5 (Imanishi et al., 2004) of the *S* velocity, respectively. Indeed, although the rupture velocity is usually of 90% of the *S* velocity, the presence of a tensile component in the source mechanism (Broberg, 2006) or fluids can decrease the rupture velocity (Lay et al., 2011), which can justify the use of $k = 0.12$. Using the radius source, the stress drops ($\Delta\sigma$) can be estimated from equation 3:

$$\Delta\sigma = \frac{7}{16} \frac{M_0}{r^3} \quad (3)$$

where M_o is the seismic moment.

4 Results

Ten fluid injections were performed during the experiments. Moreover, Test 3 was divided in two parts (denoted Test3-a and Test3-b) as it was performed on two successive days (Figure 6).

4.1 Contrasted Borehole Wall Hydromechanical Responses

Two hydromechanical behaviors related to contrasted permeabilities in borehole intervals can be noted (Figure 6):

1. High flow rate injections, greater than 60 L/min (see Table S1 in the supporting information), associated to low injection pressures (less than 3 MPa) are observed in Test 1 that connected to a high permeability zone through a fracture that bypassed the SIMFIP straddle packer system, and in Tests 5, 6, and 7 that are located in a high permeability zone (Figure 7e).
2. Relatively low flow rate injections of 6 to 40 L/Min, associated to relatively high injection pressures of 4 to 6 MPa, are observed in Tests 2, 3, 8, 9, 10, and 11 that are all located in low permeability zones (Figure 7e).

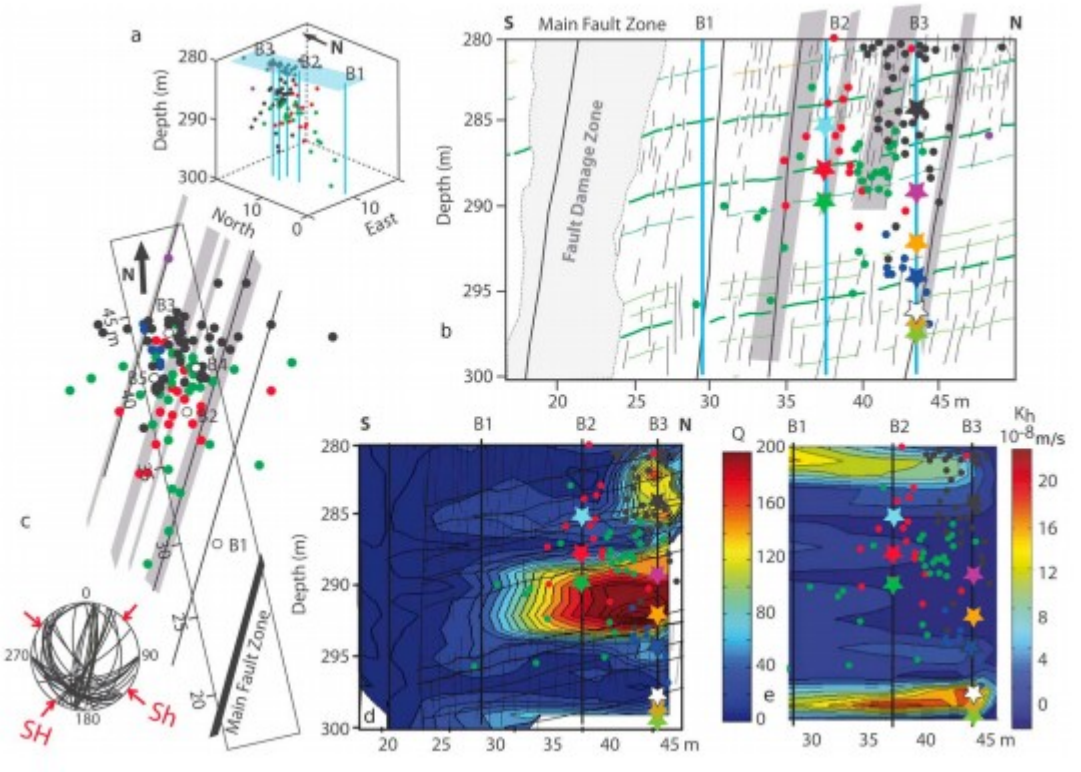

Figure 7

Location of the microseismic events. (a) 3-D view, (b) cross-section parallel to the gallery, (c) map view, (d) map of the rock quality *Q* variations performed from the data obtained on the gallery wall and on boreholes, and (e) map of the hydraulic permeability variations estimated from hydraulic tests (after Jeanne, Guglielmi, Lamarche, et al., 2012 modified). In all figures, the circles represent seismic events location with colors according to tests (red for Test 2, green for Test 3, pink for Test 8, blue for Test 9, orange for Test 10, and black for Test 11). The stars show the injection points whose colors refer to test number.

Moreover, the highest borehole displacements (see Table S1 in the supporting information) are observed in intervals where the highest injection pressure and lowest injection flow rate were imposed. This suggests a correlation between the maximum formation strain and the lowest intervals permeability.

Figure 4 shows the northern versus eastern borehole wall displacements during injections for each test (t_0 is the injection start and t_f is the injection end; continuous line represents the step-up pressure and discontinuous line the step-down pressures). Whatever is the considered test, displacements initiate along a N130° trend, which can be interpreted as the poroelastic response of the borehole (see Figure 3 for the example of Test 9). Then, they deviate more or less progressively from this initial tendency to a N60° (Tests 2, 3, 5, 7, and 9) to N90° (Tests 8 and 11) trend. Test 10, thus, in intact rock shows a poor deviation from the initial N130° trend. Tests 8 and 11 indicate deviations from N130° to N90° at (−55, 28 μm) and (−75, 53 μm), which occur at pressures of 4.4 and 5.13 MPa, respectively. This change in the horizontal displacement may be related with the normal displacement of

N10°–71°E fractures affecting the intervals. Test 9 shows a reorientation at (−30, 30 μm) to a N60° trend in good accordance with a reverse shear on the N145°-26°SW bedding plane affecting this interval, for a pressure equals to 5.25 MPa. Similar reorientations are observed in Tests 2, 3, 5 (17.0 m), and 7 (17.7 m) but on a more episodic way. Test 6 shows a different trend that can be related to the local complexity of the interval geology, which is a karstified highly fractured zone.

It is striking to observe that the initial N130° trend aligns parallel to the orientation of the bedding planes and to the direction of the minimum horizontal stress. This underlines a coupled influence of stress and sedimentary layering on the borehole poroelastic response. Deviation from this trend, occurring at high pressures, highlights the preferential displacement of N30° to N170° natural preexisting discontinuities affecting the intervals. Considering the average direction and dip direction of the potentially activated fracture in each interval, significant shear and normal displacements induced by fluid injections in intervals 2, 3, 8, 9, 10, and 11 are computed. A significant nonreversible deformation, with a shearing and/or a normal motion, is observed for all tests (see Table S1 in the supporting information).

4.2 Induced Seismicity

The detection phase identified 215 seismic events mainly spread in six tests (Tests 2, 3, 8, 9, 10, and 11). The seismicity is unequally distributed among tests (see Table S1 in the supporting information). Some of them do not show seismicity (Tests 6 and 7) or only few seismic events are detected (1 and 9 events for Tests 8 and 10, respectively). Others present a moderate seismicity (about 20 events) as Tests 2 and 9. Finally, the third and eleventh injections induced the most intense seismic activity of the experiments, with 48 and 117 seismic events, respectively.

Figure 5 presents the filtered (600–3000 Hz) signal of one of the largest events that occurred during the ninth test and recorded by one borehole accelerometer. The small delay time (smaller than 5 ms) between the *P* and *S* waves implies that both of them are intertwined, which prevents to perfectly separating both phases for the spectral analysis. Moreover, the waveform displays a resonating coda that may be due to the borehole resonance (Figure 5a). The spectrogram (Figure 5b) underlines a high-frequency content as it reaches a maximum value of about 4 kHz. This high-frequency content justifies the use of accelerometers as they can record higher frequencies than geophones. Finally, the spectrum shape (Figure 5c) is qualitatively consistent with a Brune model (Brune, 1970) in acceleration, which therefore justify the spectral analysis.

Seismicity is only observed for high pressures (>3 MPa) during the injection times as indicated in the Figure 6, where pressure, flow rate, and the occurrence of detected events are presented as a function of time. The lack of seismicity during Tests 1, 5, 6, and 7 could be due to a low fluid pressure

as it stays smaller than 3 MPa, and thus related to the high permeability of these test intervals. Figure 6 also highlights that seismic events mostly occurred at the beginning of the injections (in the phase B of the protocol; Figure 2c). For example, eight events were recorded in the six first minutes after the injection beginning in Test3-b while just one event is observed later in the test (i.e., 1h37). Fewer events happened once injections were ending. Moreover, there is no clear relationship between the displacement measured in the injection chamber and the number of seismic events. Test 11 shows the largest nonreversible displacements (77.4 µm) and the largest number of events (117) of all tests. However, a nonreversible displacement of 74.6 µm is measured during Test 10 associated to one seismic event.

Among the entire series of detected seismic events, 137 events have been absolutely or relatively located with a mean accuracy of 1.5 m. The small number of events in Tests 8 and 10 does not allow a relative location as they do not cross correlate between each other. This is why they are not taken into account in the following interpretation. Eighty-five percent of the seismic events occurred at distance greater than 2 ± 1.5 m from the injection (Figure 6). Even considering an error of 1.5 m in the location, they cannot be located on the injection chamber. Therefore, a significant lack of events is observed in the vicinity of the injection, except for the Test 9 where events might be located close to the injection chamber.

The spatial distribution of the seismicity is illustrated in Figure 7. About 80% of the seismicity is concentrated in a volume 5 m × 6 m × 18 m (Figure 7a). The seismicity repartition with depth shows that between 65% and 78% of the seismic events during Tests 2, 3, and 9 occur above their respective injection point. Test 11 shows half of the earthquakes happening below the injection interval and the other half is above. Among these last events, half of them occurred at less than 1 m below the gallery floor within the excavation damage zone. Because these events might be strongly affected by the tunnel influence, they will not be considered to interpret the spatial distribution of seismicity.

The seismicity location can be related to geological structures and characteristics of the rock medium. Figures 7b and 7c show that the events align along natural secondary faults or fracture zones with an average N20° orientation and ~70°-to-80° dip angle. Figure 7c shows a second order N90° to N100° spreading of the events during Tests 3 and 11, mainly, that may highlight a dilatation of the injected volume in the direction of the minimum principal stress. In Figure 7d, we plotted the location of the events on a map of the rock quality factor (Q-value, (Barton, 2002)) that was estimated on cores and on gallery walls by Jeanne, Guglielmi, Lamarche, et al. (2012). It clearly appears that most of the events are located in low-quality rock ($Q <$ 90–100) corresponding to highly fractured and less-than-5% porosity layers. Only a small amount of events are located in high-quality rock ($Q >$ 130) that correspond to slightly-to-un-fractured high ~20% porosity rocks. Comparing the rock quality map (Figure 7d) with the estimated permeability map

(Figure 7e), we conclude that events occurred in highly fractured but zones with low bulk permeability.

Analysis of seismic data allows estimating seismic moments varying from 0.77 to 27.3 kN m over an estimated corner frequency range comprised between 1 and 1.7 kHz (see Figure S3in the supporting information). Assuming a rupture velocity equals to 90% of the *S* wave velocity, the source radius is found to be between 0.31 to 0.57 m with stress drops between 2.5 and 178 kPa and a mean value of 17.9 kPa, whereas a rupture velocity equals to 50% of the *S* velocity drives to the source radius between 0.19 and 0.32 m (see Table S2 in the supporting information), stress drops between 13 kPa and 0.95 MPa, and a mean value of 95.8 kPa. Whatever the considered velocity rupture, stress drops are at least 1 order of magnitude smaller than those expected for tectonic events that are generally greater than 1 MPa (Kanamori & Anderson, 1975). Such small values were observed in fluid injection areas as in Barnet Shale (2.5 kPa) and Cotton Valley (16.5 kPa) (Shapiro, Krüger, & Dinske, 2013).

We determine that the moment magnitudes vary between −4.2 and −3.14. Most of them (63%) are between −3.5 and −3.9. Using the same processing approach than the ones used for seismic events, an equivalent moment magnitude was estimated for the noise. As it is found lower than −4, noise does not seem to bias the magnitude estimation. The moment magnitudes estimated for our injection experiments are smaller than the ones calculated in reservoir (oil and gas as well as geothermal sites) stimulations where moment magnitudes are classically between −3 and 2 (Shapiro, Dinske, & Kummerow, 2007). Moment magnitude evolution versus the distance between an event and its closest sensor were analyzed (see Figure S4 in the supporting information). When this distance is smaller than 2 m, seismic events with magnitude of −4.2 can be detected. Then, at 6 m distance, the threshold detection is estimated around $M_w = -4$. Consequently, the completeness magnitude is evaluated to be around $M_w = -4$ in the vicinity of the injection. Even if events with a small magnitude and located outside the experiment area can be missed, we are rather confident that all events with a magnitude greater than −4 are detected close to the injections.

In addition to those fast-slip, seismic signatures, we have also looked for lower frequency signals, which can be associated either to fluid-filled cavity resonance or to slow-velocity failure. Using both geophones (down to 10 Hz) and accelerometers (down to 2 Hz), and assuming meter-scale failures, dynamic failures as slow as a few tens of m/s (equation 2) could theoretically be seen. However, no low-frequency signatures were detected, either by threshold method or by eye-screening. Therefore, we later refer seismicity to the dynamic, fast-slip events, and aseismic motion to the slow displacement that cannot be seen by any seismic sensors.

5 Discussion

5.1 A Large Contribution of the Aseismic Deformations

Ten high-pressure fluid injections were performed to study the seismic and hydromechanical responses of different parts of the fractured damage zone of a fault zone in limestone rocks. For the entire series of injection tests, deformation data underline a nonelastic deformation at the injection point as a residual displacement (see Table S1 in the supporting information) is measured. The number of seismic events, however, strongly differs between the tests. Some tests (6, 7, and 8) show no or very little seismicity, while a more numerous seismicity is observed for Tests 3 and 11. Moreover, only few seismic events seem to be located at the injection chamber even if mechanical failure is observed on the deformation data. This suggests that a part of the deformation may be accommodated by an aseismic motion occurring, at least, around the injection chamber.

The seismic part contribution can be estimated by computing the cumulated seismic moment for each test (see Table S2 in the supporting information). The cumulated seismic moment on the whole experiment is about 500 kN.m, a value equivalent to a moment magnitude of −2.3. An equivalent deformation moment, computed from the deformation measured at the injection point, can also be estimated. It includes both the seismic and aseismic displacements. This moment is computed as follows:

$$Mo = \mu SD, \quad (4)$$

where M_o is the equivalent moment (N.m), μ is the shear modulus (20.4 GPa), S is the rupture surface (m^2), and D is the displacement (m). In our analysis, the rupture surface is unknown, but the spatial distribution of the seismicity can be used to estimate an order of magnitudes for this zone. Assuming that the seismicity is located either around or inside the area that is moving, the minimal and maximal source-injection distance can be used to compute the smaller and larger area for this surface radius. The rough assumption of a single plane is then made to compute the surface, which ranges from 4 to 144 m^2 based on the distance between source and injection that is comprised between 2 and 12 m. Using the nonreversible shear displacement (see Table S2 in the supporting information), the equivalent shear moment is found to be between 12 MN.m and 446 MN.m for a surface of 4 and 144 m^2, respectively. This implies that the seismic part is 0.1% to 3.9% of the shear deformation. Using the total nonreversible displacement (i.e., shear and normal), the equivalent moment is found to be between 34 MN.m and 1,227 MN.m for a surface of 4 and 144 m^2, respectively. This leads to a seismic part between 0.04% and 1.4% of the total deformation. Consequently, most of the deformation is aseismic in the experiment.

This corroborates previous results obtained from in situ experiments at the same scale in different rocks. For instance, De Barros et al. (2016) found that more than 99.99% of the deformation is aseismic performing similar injection experiments in shale materials. At the laboratory scale (i.e., centimeter), Goodfellow et al. (2015) performed hydraulic fracture experiments on granite

samples under different triaxial stress and investigated the energy budget. Using acoustic emission sensors, they estimated that the seismic energy represented 4 to 8% of the injection energy, indicating that aseismic deformation is a significant term in the total energy budget.

At the hectometer to kilometer scale, geothermal sites and fluid injection areas highlighted that a strong part of the deformation is aseismic as listed in Cornet (2016). For instance, fluid injections were performed at 2,900 m depth, in 1993, in the geothermal site of Soultz-sous-Forêts (Cornet et al., 1997). Televiewer observations in the borehole show that some slip motion reached 2 cm. However, recorded seismic events were too small to correspond to such motion that suggests an aseismic motion. In the same way, Scotti and Cornet (1994) measured stress after a fluid injection at 800 m depth at Le Mayet de Montagne, France. They identified a shear stress drop that could drive to a moment magnitude greater than 3. The absence of such seismic event indicated that the slip motion was aseismic. Similar results were also established for oil and gas fields. Rutledge et al. (2004) concluded to a large aseismic component in the Cotton Valley gas field, USA, by finding similarities in the seismicity patterns with the creeping part of the San Andreas Fault. Studying two hydraulic fracturing areas (one in UK and the second in the Horn River Basin in Canada) and computing their energy and volume budgets, Maxwell (2013) underlined that the majority of the deformation is aseismic.

Moreover, such behavior can also be observed at larger scale on subduction zones and crustal faults (Avouac, 2015). For instance, studying 1 week of slow slip events from the central Ecuador subduction zone, Vallée et al. (2013) underlined the cumulated seismic moment only represented 0.2% of the total deformation, obtained from GPS instruments. In the same way, McGuire et al. (2005) showed that 85% of the slip is aseismic on the transform fault along the East Pacific Rise. Thus, our meter-scale experiment with controlled fluid injection and proximal monitoring at high frequency provides complementary and consistent insights on the partitioning between seismic and aseismic motions generated during fluid injection directly into fault zones. Figure 8a presents the seismic moment versus the injected fluid volume. A clear link between the highest magnitudes and the injected volume cannot be established for the whole experiment. However, considering tests independently from each other, Tests 3 and 9 show a dependence between the moment magnitude and the injected volume as their maximum magnitudes increase with injected volumes. McGarr (1976) proposed a linear relation between the maximum seismic moment (M_o) and the total injected volume (ΔV):

$$Mo = \mu \Delta V, \quad (5)$$

where μ is the shear modulus. According to this relationship, the maximum seismic moment should be about 41 GN.m, which is far above the value of

27 kN.m that we observed here. As this relationship is based on the assumption that all the deformation is seismic (McGarr, 2014), this confirms that a strong part of the deformation is aseismic in our experiment. Besides, the equivalent deformation moment is 2 to 4 orders of magnitude lower than the McGarr's maximum seismic moment. Another evidence of this discrepancy is illustrated in Figure 8b, which presents seismic moments versus injected volumes for a broad range of injected volumes from laboratory to reservoir scale. For injected volume greater than 10,000 m^3, the induced earthquakes have a good agreement with the moment magnitude estimated with McGarr's relationship (McGarr, 2014). Conversely, for smaller injected volume, estimated seismic moments are small and situated far below this theoretical value. Consequently, the McGarr's law does not seem to be adapted and a good proxy for this type of injection experiments at the meter scale.

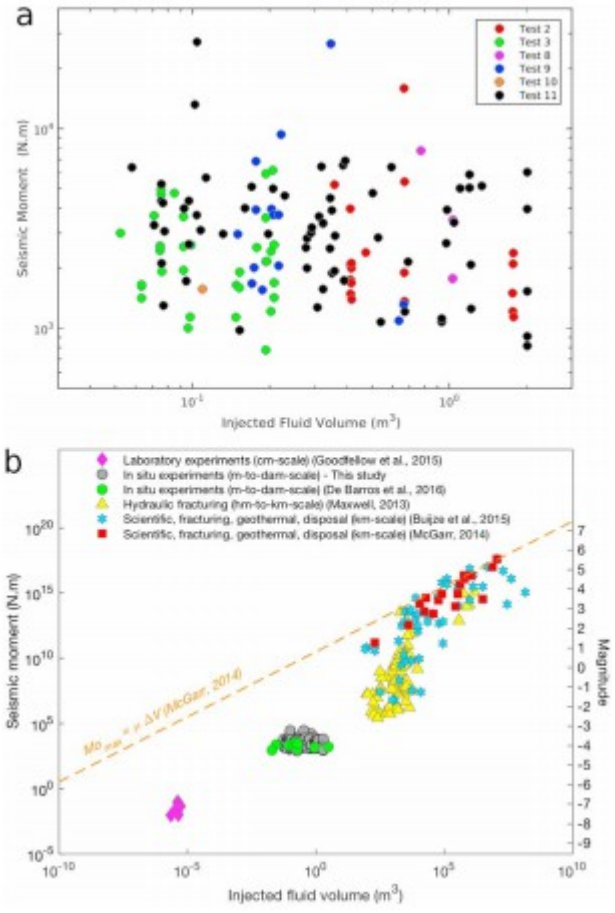

Figure 8

(a) Seismic moment versus injected fluid volume. The dots are colored according to the tests. (b) Seismic moment versus injected fluid volume for data from the laboratory scale to the crustal scale. The dotted line represents the theoretical prediction from McGarr (2014). Data are from Buijze et al. (2015), De Barros et al. (2016), Goodfellow et al. (2015), Maxwell (2013), McGarr (2014), and this study.

5.2 Seismicity Control by Fluid Diffusion or by Stress Perturbation Through Failure?

This study highlights that for a high-pressure fluid injection, most of the deformation is aseismic with only few seismic events recorded. Thus, one can wonder if the seismicity is a direct response to the fluid pressure or rather to the aseismic motion generated by injection. If the seismicity is directly triggered by the fluid pressure, the seismicity front should follow a diffusion law. The Figure 9a represents the hypocentral distances to the injection points versus time, for events occurring during injection phases. Such plots, commonly called “R-T” plot, were first used by Shapiro et al. (2002). The seismicity front is assumed to follow the pressure front according to the following equation:

$$R = \sqrt{4\pi D t}, \quad (6)$$

where the distance R is linked to the time t and the hydraulic diffusivity D. Based on this relationship, some tests can be fitted by such a law as Tests 3 and 11. Values of hydraulic diffusivities of 0.1 m^2/s and 0.005 m^2/s, respectively, can be determined, at least, for the beginning of these tests. Such values are consistent with those estimated by Shapiro et al. (2002) for the geothermal sites of Soultz-sous-Forêts (0.05 m^2/s), and the Felton Hill site (0.17 m^2/s), as well as for the KTB injection well (0.005 m^2/s; Shapiro et al., 2006). However, these diffusion coefficients are not suitable for the entire duration of the tests. The second half part of Tests 3 and 11 are fitted with respective diffusion coefficients of 0.01 m^2/s and 0.0005 m^2/s, values that are 1 order of magnitude weaker than for the first part of these two tests. This should imply that the hydraulic diffusivity of the medium decreases over the injection periods.

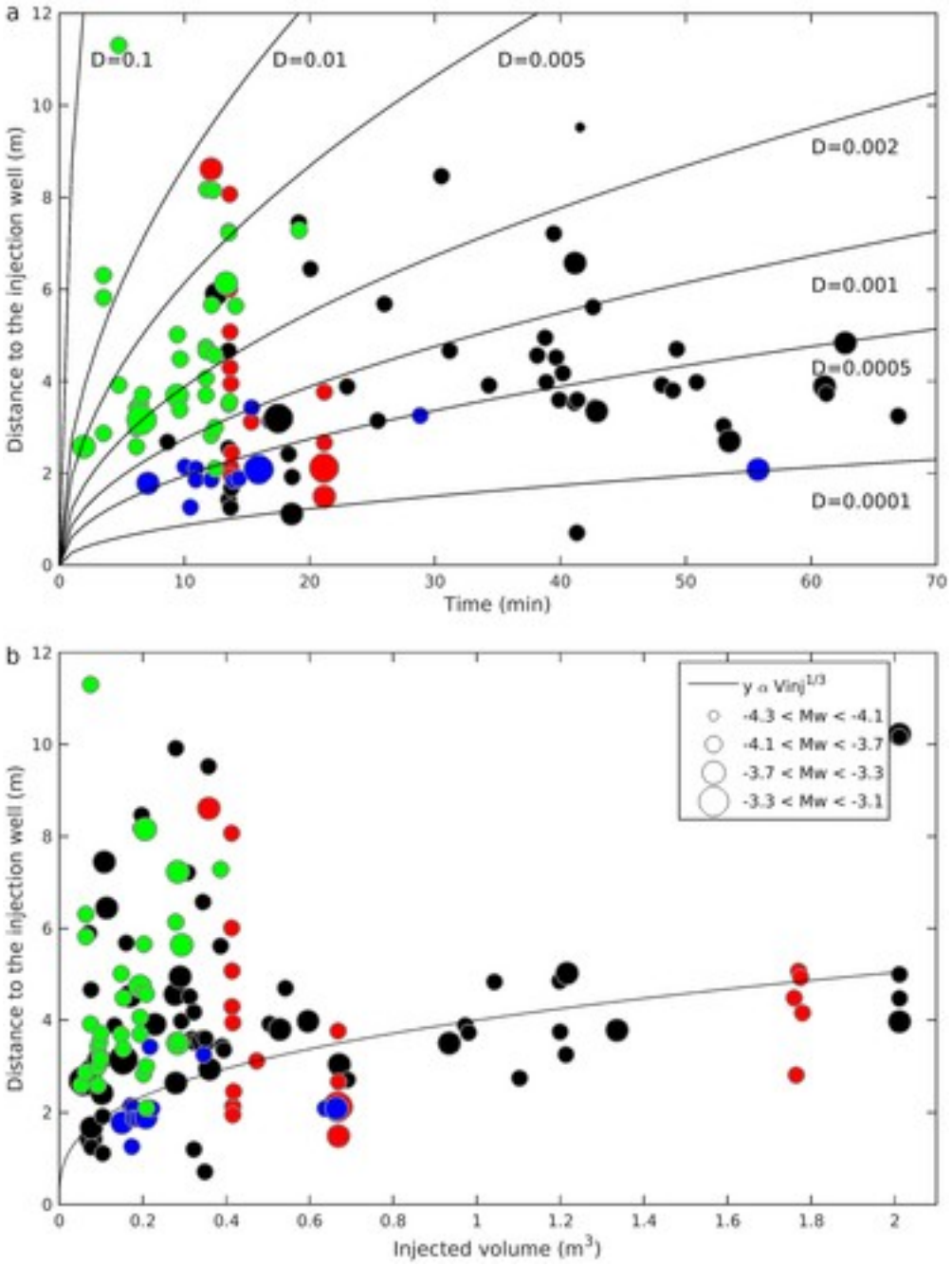

Figure 9

Hypocentral distance to the injection point of events occurring during injection period versus (a) time. The black lines represent the theoretical predictions for the seismicity front for different diffusivities (0.01, 0.005, 0.002, 0.001, 0.0005, and 0.0001 m^2/s) according to equation 6. (b) Injected volume. For both panels, the dots are colored according to the tests: red for Test 2, green for Test 3, blue for Test 9, and black for Test 11.

Thus, even if seismic events seem to follow a fluid diffusion law, our analysis shows that the diffusivity coefficient varies of 1 order of magnitude during tests. Consequently, a direct relationship between the seismicity location and the fluid front is not obvious. This is consistent with the previous study of

Cornet (2000) that asserts that when hydromechanical coupling occurred, the hypothesis of a constant homogeneous hydraulic diffusivity is not valid and the seismicity cloud growth is rather associated with the development of the fracturing or fracture reactivation process than the hydraulic diffusivity.

Moreover, the hypocentral distribution for Tests 2 and 8 does not follow a diffusion law as events are clustered in time (Figure 6), but they are rather scattered in space (Figure 7). This suggests that the controlled mechanism of this seismicity might not be directly associated with a fluid diffusion but rather with a mechanism of stress perturbation through failure in the medium. Another way to visualize these data is through Figure 9b, which shows the hypocentral distance versus the injected volume. In a poroelastic medium, the fluid distribution should geometrically spread as a cubic root of the injected volume (ΔV). If the seismicity front follows the fluid front, the hypocentral distance R is

$$R \propto \sqrt[3]{\Delta V} \qquad (7)$$

Figure 9b shows that the hypocentral distance can be fitted by such a law for the seismicity that is associated with the largest injected volume. However, for the smallest injected volume, this relationship is clearly unsuitable because the source-injection distance does not depend on the injected volume. Test 11 perfectly illustrates this dual behavior: for the smallest volume, their hypocentral distance is independent of the injected volume, whereas for the largest volume, the source-injection distance increases with the injected volume. For Test 2, the seismic events appear sequentially: in the same seismic burst the distance between source and injection is independent from injected volume. Consequently, two different processes are required: for small injected volume, seismicity does not directly depend on fluid diffusion, whereas the pressure diffusion might explain the average seismicity distribution for longer injection.

Moreover, in our experiment, injections are not continuous, including several injection stages in a same test (Figure 6). For example, during the Test3-a, four distinct injection periods (Figure 6) were performed and seismicity only occurred at the beginning of these periods. The same pattern is observed on Tests 2 and for the first half part of Test 11. Thus, the seismicity only occurred after the increase of pressure. This could suggest that the seismicity is related to the pressure changes rather than to the pressure level. Finally, some events occurred after the injections. This phenomena was previously observed in different fluid injection areas, such as the geothermal fields at Basel (Bachmann et al., 2011), and Berlín, in San Salvador (Kwiatek et al., 2014), where the largest event happened some hours and 2 weeks after the injection ending, respectively. These events can be explained by strain relaxation in the medium (Mukuhira et al., 2013) or by a fluid diffusion and related stress perturbation through failure still acting

after the injection end (Baisch et al., 2006; McClure & Horne, 2011; Segall & Lu, 2015).

5.3 Seismicity: An Indirect Effect of an Aseismic Motion?

In our experiment, the comparison of seismic and hydromechanical data indicates that the relationship between fluids and seismicity is not a trivial cause-and-effect link supported by the following observations:

1. the large amount of aseismic motion, particularly in the vicinity of the injection;
2. the temporal clustering of the events at the beginning of the injections; and
3. the dual seismicity patterns with respect to fluid diffusion.

Therefore, a complex model is required to explain this behavior. First, deformation data and the lack of seismicity at the injection points show that most of the deformations directly induced by fluid pressure are aseismic. Observed seismic events might just be a response to this aseismic deformation that modifies the stress field in the volume around it. The seismicity is thus an indirect effect of the fluid pressurization. Guglielmi et al. (2015), who performed similar experiments with a limited seismic network compared to the present study, have already observed that aseismic slip started before the seismicity occurs and interpreted the triggered seismicity as an indirect effect mediated by the aseismic motion. Here we confirmed such behavior based on a detailed seismic analysis. Similar conclusions were also supported by De Barros et al. (2016) in shale materials. At larger scale, Wei et al. (2015) studied the seismicity associated with a fluid injection in the Brawley geothermal field, California. Two large earthquakes ($M_w > 5$) were recorded in 2012 and located several kilometers below the injection zones. This study also shows that the injection induced a large aseismic slip on a fault, which in turn has triggered the earthquakes on a secondary fault. Thus, consistently with the meter-scale experiments, this study highlighted that seismic events are an indirect effect driven by the injection-induced aseismic slip.

Second, for longer injection time, the aseismic motion increases the fracture permeability and might open new paths for fluids. Therefore, a new volume has to be saturated and pressurized before reaching a new aseismic failure, which in turn might drive seismic events. The induced seismicity will therefore extend further than in the first phase of failure leading to an apparent diffusivity. However, this second series of failures was only observed during Test 11, where a diffusive pattern was evidenced. For the other tests, no seismicity is observed after the first seismic cluster in the longest injections. This might be only due to an insufficient injected volume and flow to pressurize and reach failures in the newly created larger volume. This is the case in the Tests 5, 6, and 7 where fluid pressure remains low. Finally, seismicity occurred after every increase of pressure following a

pressure drop. This could suggest that after every increase of pressure following a pressure drop, the aseismic slip is reactivated, leading to an increase of stress perturbation through failure and new seismic events.

In summary, failures induced by the fluid pressure are mainly aseismic. This aseismic motion (1) can create new hydraulic paths for fluids (and therefore opening a larger volume to pressurize) and (2) may trigger seismicity by stress perturbation through failure, which might be away from the saturated zone. As these failures repeat for increasing volume when injection is going-on, the seismic cloud increases, and seems to follow a fluid diffusion. This might be the case for injections in Soultz-sous-Forêts or in Fenton Hill, where the seismicity occurred clustered in time, but followed a diffusion law over the long term range (Shapiro et al., 2002). A similar pattern is observed on the wastewater disposal of the oil and field production of High Agri Valley in the South of Italy (Stabile et al., 2014). Moreover, the microseismic events are generally used to follow the fluid diffusion in the reservoir monitoring. This study shows that microearthquakes might be more representative of local change in the stress field controlled by the heterogeneity of structural properties than of the location of the fluid pressure change. Consequently, this monitoring tool has to be cautiously interpreted as containing mixed information on fluid, stress, and structural properties.

6 Conclusion

In this study, we have developed a meter-scale in situ fluid injection experiment at 280 m depth within the fractured damage zone of a normal fault in carbonate rocks. We have used a dense and proximal monitoring at high frequency of seismicity coupled with fluid pressure and fault displacement measurements at the injection and took advantage of 10 hydraulic stimulations in different parts of a fractured damage zone to explore the seismic and aseismic responses to the fluid perturbation. Although pressures at a level comparable with the initial state of stress were injected and that different fractures and faults were reactivated, only a sparse seismicity (215 events) was recorded. Through our interpretations of experimental data, the comparison of the cumulated seismic moment with the deformation energy indicates that less than 4% of the deformation is seismic. Thus, our study indicates that most deformations induced by injections are aseismic. Moreover, a simple diffusion patterns cannot explain the spatiotemporal distribution of the seismicity, which is clearly related to structural heterogeneity. We find that the injected fluid saturates and pressurizes a fracture network around the well. Once a pressure threshold is reached, aseismic motions occur. These deformations modify the stress around the saturated zone, leading to seismic failures by stress perturbation and/or to stress concentration effects at the boundaries between different rock types. The aseismic deformation also increases the fracture permeability, creating new paths for the fluids. The volume to saturate and pressurize becomes larger, leading to new aseismic failures once the pressure threshold is reached. Therefore, we find that the seismicity

observed in our experiment is not directly induced by the injected pressure but is likely a response to the stress transferred from the aseismic motion. Additionally, we find that the relationship between the seismic moment and the injected fluid volume does not follow the conventional McGarr's law, highlighting that additional mechanisms are involved. We suggest that large aseismic deformations could explain this apparent discrepancy.

More importantly, our study shows that injection-induced aseismic motions play a crucial role for both the fluid pressure diffusion and the distribution of seismicity. Thus, aseismic motions should be accurately measured during fluid injections and considered with great care in the analyses of induced and triggered seismicity.

Acknowledgments

This work was funded by the Agence Nationale de la Recherche (ANR) through the HYDROSEIS project under contract ANR-13-JS06-0004-01 (PI. F. Cappa) and by Total SA through the HPMS-Ca project (Albion, PI. G. Massonat). SITES company (J. Durand, H. Caron, and Y. Zouhair) is acknowledged for installing and maintaining the SIMFIP probe, sensors, and acquisition during the experiment. We thank E. Larose and L. Stehly (ISTERRE) for the help with sensors. We thank the LSBB and its technical support for logistical help during the experiment. F. Cappa thanks S. Goodfellow for providing his laboratory data used in Figure 8b. We are very grateful to François Cornet, an anonymous reviewer, and the Editor, Yehuda Ben Zion, for the constructive comments and recommendations that helped us to improve the original version of our work. All experimental data are stored in the Géoazur laboratory (Université Côte d'Azur, CNRS, OCA, IRD) and are available upon request (contact: louis.debarros@geoazur.unice.fr).

References

Aki, K., & Richards, P. G. (1980). *Quantitative seismology, theory and methods*, (Vol. 1). Co: *WH Free*.

Avouac, J.-P. (2015). From geodetic imaging of seismic and aseismic fault slip to dynamic modeling of the seismic cycle. *Annual Review of Earth and Planetary Sciences*, 43(1), 233– 271. https://doi.org/10.1146/annurev-earth-060614-105302

Bachmann, C. E., Wiemer, S., Goertz-Allmann, B. P., & Woessner, J. (2012). Influence of pore-pressure on the event-size distribution of induced earthquakes. *Geophysical Research Letters*, 39, L09302. https://doi.org/10.1029/2012GL051480

Bachmann, C. E., Wiemer, S., Woessner, J., & Hainzl, S. (2011). Statistical analysis of the induced Basel 2006 earthquake sequence: Introducing a probability-based monitoring approach for enhanced geothermal systems. *Geophysical Journal International*, 186(2), 793– 807. https://doi.org/10.1111/j.1365-246X.2011.05068.x

Baisch, S., Weidler, R., Vörös, R., & Jung, R. (2006). A conceptual model for post-injection seismicity at Soultz-sous-Forêts. *GRC Transaction*, 30, 601–605.

Bao, X., & Eaton, D. W. (2016). Fault activation by hydraulic fracturing in western Canada. *Science*, 354(6318), 1406– 1409. https://doi.org/10.1126/science.aag2583

Barnhart, W. D., Benz, H. M., Hayes, G. P., Rubinstein, J. L., & Bergman, E. (2014). Seismological and geodetic constraints on the 2011 M_w5.3 Trinidad, Colorado earthquake and induced deformation in the Raton Basin. *Journal of Geophysical Research: Solid Earth*, 119, 7923– 7933. https://doi.org/10.1002/2014JB011227

Barton, N. (2002). Some new Q-value correlations to assist in site characterization and tunnel design. *International Journal of Rock Mechanics and Mining Sciences*, 39(2), 185– 216. https://doi.org/10.1016/S1365-1609(02)00011-4

Boore, D. M. (1983). Stochastic simulation of high-frequency ground motions based on seismological models of the radiated spectra. *Bulletin of the Seismological Society of America*, 73(6), 1865– 1894.

Broberg, K. B. (2006). Differences between mode I and mode II crack propagation. *Pure and Applied Geophysics*, 163(9), 1867– 1879. https://doi.org/10.1007/s00024-006-0101-7

Brune, J. N. (1970). Tectonic stress and the spectra of seismic shear waves from earthquakes. *Journal of Geophysical Research*, 75(26), 4997– 5009. https://doi.org/10.1029/JB075i026p04997

Brune, J. N., Archuleta, R. J., & Hartzell, S. (1979). Far-field S-wave spectra, corner frequencies, and pulse shapes. *Journal of Geophysical Research*, 84(B5), 2262– 2272. https://doi.org/10.1029/JB084iB05p02262

Buijze, L., Orlic, B., Wassing, B. B. T., & Schreppers, G.-J. (2015). *Dynamic Rupture Modeling of Injection-Induced Seismicity: Influence of Pressure Diffusion Below Porous Aquifers*, American Rock Mechanics Association, ARMA 15-384, 49th US Rock Mechanics/Geomechanics Symposium held in San Francisco, CA, 28 June – 1 July 2015.

Calò, M., Dorbath, C., Cornet, F. H., & Cuenot, N. (2011). Large-scale aseismic motion identified through 4-D P-wave tomography. *Geophysical Journal International*, 186(3), 1295– 1314. https://doi.org/10.1111/j.1365-246X.2011.05108.x

Cappa, F., Rutqvist, J., & Yamamoto, K. (2009). Modeling crustal deformation and rupture processes related to upwelling of deep CO_2-rich fluids during the 1965–1967 Matsushiro earthquake swarm in Japan. *Journal of Geophysical Research*, 114, B10304. https://doi.org/10.1029/2009JB006398

Cornet, F. H. (2000). Comment on “Large-scale in situ permeability tensor of rocks from induced microseismicity” by S. A. Shapiro, P. Audigane and J.-J. Royer. *Geophysical Journal International*, 140(2), 465– 469. https://doi.org/10.1046/j.1365-246x.2000.00018.x

Cornet, F. H. (2012). The relationship between seismic and aseismic motions induced by forced fluid injections. *Hydrogeology Journal*, 20(8), 1463– 1466. https://doi.org/10.1007/s10040-012-0901-z

Cornet, F. H. (2016). Seismic and aseismic motions generated by fluid injections. *Geomechanics for Energy and the Environment*, 5, 42– 54. https://doi.org/10.1016/j.gete.2015.12.003

Cornet, F. H., Helm, J., Poitrenaud, H., & Etchecopar, A. (1997). Seismic and aseismic slips induced by large-scale fluid injections. In S Talebi (Ed.), *Seismicity associated with mines, reservoirs and fluid injections* (pp. 563–583). Basel: Birkhäuser Basel. https://doi.org/10.1007/978-3-0348-8814-1_12

Cuenot, N., Dorbath, C., & Dorbath, L. (2008). Analysis of the microseismicity induced by fluid injections at the EGS site of Soultz-sous-Forêts (Alsace, France): Implications for the characterization of the geothermal reservoir properties. *Pure and Applied Geophysics*, 165(5), 797– 828. https://doi.org/10.1007/s00024-008-0335-7

Daniel, G. (2014). Bias in magnitude for earthquakes with unknown focal mechanism. *Geophysical Prospecting*, 62(4), 848– 861. https://doi.org/10.1111/1365-2478.12142

De Barros, L., Daniel, G., Guglielmi, Y., Rivet, D., Caron, H., Payre, X., … Gourlay, M. (2016). Fault structure, stress, or pressure control of the seismicity in shale? Insights from a controlled experiment of fluid-induced fault reactivation. *Journal of Geophysical Research: Solid Earth*, 121, 4506–4522. https://doi.org/10.1002/2015JB012633

Derode, B., Guglielmi, Y., De Barros, L., & Cappa, F. (2015). Seismic responses to fluid pressure perturbations in a slipping fault. *Geophysical Research Letters*, 42(9), 3197– 3203. https://doi.org/10.1002/2015GL063671

Duverger, C., Godano, M., Bernard, P., Lyon-Caen, H., & Lambotte, S. (2015). The 2003–2004 seismic swarm in the western Corinth rift: Evidence for a multiscale pore pressure diffusion process along a permeable fault system. *Geophysical Research Letters*, 42, 7374– 7382. https://doi.org/10.1002/2015GL065298

Ellsworth, W. L. (2013). Injection-induced earthquakes. *Science*, 341(6142). https://doi.org/10.1126/science.1225942

Ellsworth, W. L., Llenos, A. L., McGarr, A. F., Michael, A. J., Rubinstein, J. L., Mueller, C. S., … Calais, E. (2015). Increasing seismicity in the U. S. midcontinent: Implications for earthquake hazard. *The Leading Edge*, 34(6), 618– 626. https://doi.org/10.1190/tle34060618.1

Elsworth, D., Spiers, C. J., & Niemeijer, A. R. (2016). Understanding induced seismicity. *Science*, 354(6318), 1380– 1381. https://doi.org/10.1126/science.aal2584

Eshelby, J. D. (1957). The determination of the elastic field of an ellipsoidal inclusion, and related problems. *Proceedings of the Royal Society London A: Mathematical, Physical and Engineering Sciences*, 241(1226), 376– 396. https://doi.org/10.1098/rspa.1957.0133

Goebel, T. H. W., Weingarten, M., Chen, X., Haffener, J., & Brodsky, E. E. (2017). The 2016 M_w5.1 Fairview, Oklahoma earthquakes: Evidence for long-range poroelastic trigerring at >40 km from fluid disposal wells. *Earth and Planetary Science Letters*, 472, 50– 61. https://doi.org/10.1016/j.epsl.2017.05.011

Goodfellow, S. D., Nasseri, M. H. B., Maxwell, S. C., & Young, R. P. (2015). Hydraulic fracture energy budget: Insights from the laboratory. *Geophysical Research Letters*, 42(9), 3179– 3187. https://doi.org/10.1002/2015GL063093

Guglielmi, Y., Cappa, F., Avouac, J.-P., Henry, P., & Elsworth, D. (2015). Seismicity triggered by fluid injections induced aseismic slip. *Science*, 348(6240), 1224– 1226. https://doi.org/10.1126/science.aab0476

Guglielmi, Y., Cappa, F., Lancon, H., Janowczyk, J., Rutqvist, J., Tsang, C.-F., & Wang, J. S. Y. (2013). ISRM suggested method for Step-Rate Injection Method for Fracture In-Situ Properties (SIMFIP): Using a 3-components borehole deformation sensor. *Rock Mechanics and Rock Engineering*, 47(1), 303– 311. https://doi.org/10.1007/s00603-013-0517-1

Haimson, B. C., & Cornet, F. H. (2003). ISRM suggested methods for rock stress estimation—Part 3: Hydraulic fracturing (HF) and/or hydraulic testing of pre-existing fractures (HTPF). *International Journal of Rock Mechanics and Mining Sciences*, 40(7-8), 1011– 1020. https://doi.org/10.1016/j.ijrmms.2003.08.002

Hainzl, S. (2004). Seismicity patterns of earthquake swarms due to fluid intrusion and stress triggering. *Geophysical Journal International*, 159(3), 1090– 1096. https://doi.org/10.1111/j.1365-246X.2004.02463.x

Hainzl, S., Kraft, T., Wassermann, J., Igel, H., & Schmedes, E. (2006). Evidence for rainfall-triggered earthquake activity. *Geophysical Research Letters*, 33, L19303. https://doi.org/10.1029/2006GL027642

Healy, J. H., Rubey, W. W., Griggs, D. T., & Raleigh, C. B. (1968). The Denver earthquakes. *Science*, 161(3848), 1301– 1310. https://doi.org/10.1126/science.161.3848.1301

Hubbert, M. K., & Rubey, W. W. (1959). Role of fluid pressure in mechanics of overthrust faulting I. Mechanics of fluid-filled porous solids and its application to overthrust faulting. *Geological Society of America Bulletin*, 70(2), 115– 166.

Imanishi, K., Takeo, M., Ellsworth, W. L., Ito, H., Matsuzawa, T., Kuwahara, Y., … Ohmi, S. (2004). Source parameters and rupture velocities of microearthquakes in Western Nagano, Japan, determined using stopping phases. *Bulletin of the Seismological Society of America*, 94(5), 1762– 1780. https://doi.org/10.1785/012003085

Jeanne, P., Guglielmi, Y., & Cappa, F. (2012). Multiscale seismic signature of a small fault zone in a carbonate reservoir: Relationships between V_p imaging, fault zone architecture and cohesion. *Tectonophysics*, 554-557, 185– 201. https://doi.org/10.1016/j.tecto.2012.05.012

Jeanne, P., Guglielmi, Y., Lamarche, J., Cappa, F., & Marié, L. (2012). Architectural characteristics and petrophysical properties evolution of a strike-slip fault zone in a fractured porous carbonate reservoir. *Journal of Structural Geology*, 44, 93– 109. https://doi.org/10.1016/j.jsg.2012.08.016

Kanamori, H., & Anderson, D. L. (1975). Theoretical basis of some empirical relations in seismology. *Bulletin of the Seismological Society of America*, 65(5), 1073– 1095.

Kaneko, Y., & Shearer, P. M. (2014). Seismic source spectra and estimated stress drop derived from cohesive-zone models of circular subshear rupture. *Geophysical Journal International*, 197(2), 1002– 1015. https://doi.org/10.1093/gji/ggu030

Kayal, J. R., Zhao, D., Mishra, O. P., De, R., & Singh, O. P. (2002). The 2001 Bhuj earthquake: Tomographic evidence for fluids at the hypocenter and its implications for rupture nucleation, *Geophysical Research Letters*, 29(24), 4– 5, 2152. https://doi.org/10.1029/2002GL015177

Keranen, K. M., Savage, H. M., Abers, G. A., & Cochran, E. S. (2013). Potentially induced earthquakes in Oklahoma, USA: Links between wastewater injection and the 2011 M_w 5.7 earthquake sequence. *Geology*, 41(6), 699– 702. https://doi.org/10.1130/G34045.1

Keranen, K. M., Weingarten, M., Abers, G. A., Bekins, B. A., & Ge, S. (2014). Sharp increase in central Oklahoma seismicity since 2008 induced by massive wastewater injection. *Science*, 345(6195), 448– 451. https://doi.org/10.1126/science.1255802

Kwiatek, G., Bulut, F., Bohnhoff, M., & Dresen, G. (2014). High-resolution analysis of seismicity induced at Berlín geothermal field, El Salvador. *Geothermics*, 52, 98– 111. https://doi.org/10.1016/j.geothermics.2013.09.008

Lay, T., Yamazaki, Y., Ammon, C. J., Cheung, K. F., & Kanamori, H. (2011). The 2011 M_w 9.0 off the Pacific coast of Tohoku earthquake: Comparison of deep-water tsunami signals with finite-fault rupture model predictions. *Earth, Planets and Space*, 63(7), 797– 801. https://doi.org/10.5047/eps.2011.05.030

Leclère, H., Fabbri, O., Daniel, G., & Cappa, F. (2012). Reactivation of a strike-slip fault by fluid overpressuring in the southwestern French-Italian

Alps. *Geophysical Journal International*, 189(1), 29– 37. https://doi.org/10.1111/j.1365-246X.2011.05345.x

Lengliné, O., Boubacar, M., & Schmittbuhl, J. (2017). Seismicity related to the hydraulic stimulation of GRT1, Rittershoffen, France. *Geophysical Journal International*, 208(3), ggw490. https://doi.org/10.1093/gji/ggw490

Madariaga, R. (1977). High-frequency radiation from crack (stress drop) models of earthquake faulting. *Geophysical Journal of the Royal Astronomical Society*, 51(3), 625– 651. https://doi.org/10.1111/j.1365-246X.1977.tb04211.x

Maxwell, S. C. (2013). Unintentional seismicity induced by hydraulic fracturing, CSEG Rec., 38(8).

McClure, M. W., & Horne, R. N. (2011). Investigation of injection-induced seismicity using a coupled fluid flow and rate/state friction model. *Geophysics*, 76(6), WC181– WC198. https://doi.org/10.1190/geo2011-0064.1

McGarr, A. (1976). Seismic moments and volume changes. *Journal of Geophysical Research*, 81(8), 1487– 1494. https://doi.org/10.1029/JB081i008p01487

McGarr, A. (2014). Maximum magnitude earthquakes induced by fluid injection. *Journal of Geophysical Research: Solid Earth*, 119, 1008– 1019. https://doi.org/10.1002/2013JB010597

McGarr, A., Bekins, B., Burkardt, N., Dewey, J., Earle, P., Ellsworth, W., … Sheehan, A. (2015). Coping with earthquakes induced by fluid injection. *Science*, 347(6224), 830– 831. https://doi.org/10.1126/science.aaa0494

McGuire, J. J., Boettcher, M. S., & Jordan, T. H. (2005). Foreshock sequences and short-term earthquake predictability on East Pacific Rise transform faults. *Nature*, 434(7032), 457– 461. https://doi.org/10.1038/nature03377

McNamara, D. E., Benz, H. M., Herrmann, R. B., Bergman, E. A., Earle, P., Holland, A., … Gassner, A. (2015). Earthquake hypocenters and focal mechanisms in central Oklahoma reveal a complex system of reactivated subsurface strike-slip faulting. *Geophysical Research Letters*, 42, 2742– 2749. https://doi.org/10.1002/2014GL062730

Miller, S. A. (2008). Note on rain-triggered earthquakes and their dependence on karst geology. *Geophysical Journal International*, 173(1), 334– 338. https://doi.org/10.1111/j.1365-246X.2008.03735.x

Mukuhira, Y., Asanuma, H., Niitsuma, H., & Häring, M. O. (2013). Characteristics of large-magnitude microseismic events recorded during and after stimulation of a geothermal reservoir at Basel, Switzerland. *Geothermics*, 45, 1– 17. https://doi.org/10.1016/j.geothermics.2012.07.005

Norbeck, J. H., & Horne, R. N. (2016). Evidence for a transient hydromechanical and frictional faulting response during the 2011 M_w 5.6

Prague, Oklahoma earthquake sequence. *Journal of Geophysical Research: Solid Earth*, 121, 8688– 8705. https://doi.org/10.1002/2016JB013148

Pacchiani, F., & Lyon-Caen, H. (2010). Geometry and spatio-temporal evolution of the 2001 Agios Ioanis earthquake swarm (Corinth Rift, Greece). *Geophysical Journal International*, 180(1), 59– 72. https://doi.org/10.1111/j.1365-246X.2009.04409.x

Parotidis, M., Rothert, E., & Shapiro, S. A. (2003). Pore-pressure diffusion: A possible triggering mechanism for the earthquake swarms 2000 in Vogtland/ NW-Bohemia, central Europe, *Geophysical Research Letters*, 30(20), 2075. https://doi.org/10.1029/2003GL018110

Petersen, M. D., Mueller, C. S., Moschetti, M. P., Hoover, S. M., Llenos, A. L., Ellsworth, W. L., … Rukstales, K. S. (2016). Seismic-hazard forecast for 2016 including induced and natural earthquakes in the central and eastern United States. *Seismological Research Letters*, 87(6), 1327– 1341. https://doi.org/10.1785/0220160072

Rigo, A., Béthoux, N., Masson, F., & Ritz, J.-F. (2008). Seismicity rate and wave-velocity variations as consequences of rainfall: The case of the catastrophic storm of September 2002 in the Nîmes Fault region (Gard, France). *Geophysical Journal International*, 173(2), 473– 482. https://doi.org/ 10.1111/j.1365-246X.2008.03718.x

Rivet, D., De Barros, L., Guglielmi, Y., Cappa, F., Castilla, R., & Henry, P. (2016). Seismic velocity changes associated with aseismic deformations of a fault stimulated by fluid injection. *Geophysical Research Letters*, 43, 9563– 9572. https://doi.org/10.1002/2016GL070410

Ruina, A. (1983). Slip instability and state variable friction laws. *Journal of Geophysical Research: Solid Earth*, 88(B12), 10359– 10370. https://doi.org/10.1029/JB088iB12p10359

Rutledge, J. T., Phillips, W. S., & Mayerhofer, M. J. (2004). Faulting induced by forced fluid injection and fluid flow forced by faulting: An interpretation of hydraulic-fracture microseismicity, Carthage Cotton Valley gas field, Texas. *Bulletin of the Seismological Society of America*, 94(5), 1817– 1830. https://doi.org/10.1785/012003257

Schmittbuhl, J., Lengliné, O., Cornet, F., Cuenot, N., & Genter, A. (2014). Induced seismicity in EGS reservoir: The creep route. *Geothermal Energy*, 2(1), 1– 13. https://doi.org/10.1186/s40517-014-0014-0

Scotti, O., & Cornet, F. H. (1994). In situ evidence for fluid-induced aseismic slip events along fault zones. *International Journal of Rock Mechanics and Mining Science and Geomechanics Abstracts*, 31(4), 347– 358. https://doi.org/10.1016/0148-9062(94)90902-4

Segall, P., & Lu, S. (2015). Injection-induced seismicity: Poroelastic and earthquake nucleation effects. *Journal of Geophysical Research: Solid Earth*, 120, 5082– 5103. https://doi.org/10.1002/2015JB012060

Shapiro, S. A., Dinske, C., & Kummerow, J. (2007). Probability of a given-magnitude earthquake induced by a fluid injection. *Geophysical Research Letters*, 34, L22314. https://doi.org/10.1029/2007GL031615

Shapiro, S. A., Krüger, O. S., & Dinske, C. (2013). Probability of inducing given-magnitude earthquakes by perturbing finite volumes of rocks. *Journal of Geophysical Research: Solid Earth*, 118, 3557– 3575. https://doi.org/10.1002/jgrb.50264

Shapiro, S. A., Kummerow, J., Dinske, C., Asch, G., Rothert, E., Erzinger, J., … Kind, R. (2006). Fluid induced seismicity guided by a continental fault: Injection experiment of 2004/2005 at the German Deep Drilling Site (KTB). *Geophysical Research Letters*, 33, L01309. https://doi.org/10.1029/2005GL024659

Shapiro, S. A., Rothert, E., Rath, V., & Rindschwentner, J. (2002). Characterization of fluid transport properties of reservoirs using induced microseismicity. *Geophysics*, 67(1), 212– 220. https://doi.org/10.1190/1.1451597

Shearer, P. M. (1997). Improving local earthquake locations using the L1 norm and waveform cross correlation: Application to the Whittier Narrows, California, aftershock sequence. *Journal of Geophysical Research*, 102(B4), 8269– 8283. https://doi.org/10.1029/96JB03228

Shelly, D. R., Taira, T., Prejean, S. G., Hill, D. P., & Dreger, D. S. (2015). Fluid-faulting interactions: Fracture-mesh and fault-valve behavior in the February 2014 Mammoth Mountain, California, earthquake swarm. *Geophysical Research Letters*, 42, 5803– 5812. https://doi.org/10.1002/2015GL064325

Stabile, T. A., Giocoli, A., Perrone, A., Piscitelli, S., & Lapenna, V. (2014). Fluid injection induced seismicity reveals a NE dipping fault in the southeastern sector of the High Agri Valley (southern Italy). *Geophysical Research Letters*, 41, 5847– 5854. https://doi.org/10.1002/2014GL060948

Stork, A. L., Verdon, J. P., & Kendall, J.-M. (2014). The robustness of seismic moment and magnitudes estimated using spectral analysis. *Geophysical Prospecting*, 62(4), 862– 878. https://doi.org/10.1111/1365-2478.12134

Sumy, D. F., Neighbors, C. J., Cochran, E. S., & Keranen, K. M. (2017). Low stress drops observed for aftershocks of the 2011 M_w 5.7 Prague, Oklahoma earthquake. *Journal of Geophysical Research: Solid Earth*, 122, 3813– 3834. https://doi.org/10.1002/2016JB013153

Sun, X., & Hartzell, S. (2014). Finite-fault slip model of the 2011 M_w 5.6 Prague, Oklahoma earthquake from regional waveforms. *Geophysical Research Letters*, 41, 4207– 4213. https://doi.org/10.1002/2014GL060410

Trugman, D. T., Shearer, P. M., Borsa, A. A., & Fialko, Y. (2016). A comparison of long-term changes in seismicity at The Geysers, Salton Sea, and Coso geothermal fields. *Journal of Geophysical Research: Solid Earth*, 121, 225–247. https://doi.org/10.1002/2015JB012510

Vallée, M., Nocquet, J.-M., Battaglia, J., Font, Y., Segovia, M., Regnier, M., … Vaca, S. (2013). Intense interface seismicity triggered by a shallow slow slip event in the Central Ecuador subduction zone. *Journal of Geophysical Research: Solid Earth*, 118, 2965– 2981. https://doi.org/10.1002/jgrb.50216

Von Seggern, D. (1970). The effects of radiation patterns on magnitude estimates. *Bulletin of the Seismological Society of America*, 60(2), 503– 516.

Waldhauser, F., & Ellsworth, W. L. (2000). A double-difference earthquake location algorithm: Method and application to the northern Hayward fault, California. *Bulletin of the Seismological Society of America*, 90(6), 1353– 1368. https://doi.org/10.1785/0120000006

Walsh, F. R., & Zoback, M. D. (2015). Oklahoma's recent earthquakes and saltwater disposal. *Science Advances*, 1(5), e1500195. https://doi.org/10.1126/sciadv.1500195

Walter, W. R., Yoo, S.-H., Mayeda, K., & Gök, R. (2017). Earthquake stress via event ratio levels: Application to the 2011 and 2016 Oklahoma seismic sequences. *Geophysical Research Letters*, 44, 3147– 3155. https://doi.org/10.1002/2016GL072348

Wei, S., Avouac, J.-P., Hudnut, K. W., Donnellan, A., Parker, J. W., Graves, R. W., … Eneva, M. (2015). The 2012 Brawley swarm triggered by injection-induced aseismic slip. *Earth and Planetary Science Letters*, 422, 115– 125. https://doi.org/10.1016/j.epsl.2015.03.054

Weingarten, M., Ge, S., Godt, J. W., Bekins, B. A., & Rubinstein, J. L. (2015). High-rate injection is associated with the increase in U.S. mid-continent seismicity. *Science*, 348(6241), 1336– 1340. https://doi.org/10.1126/science.aab1345

Wilkens, R., Simmons, G., & Caruso, L. (1984). The ratio V_p/V_s as a discriminant of composition for siliceous limestones. *Geophysics*, 49(11), 1850– 1860. https://doi.org/10.1190/1.1441598

Yeck, W. L., Hayes, G. P., McNamara, D. E., Rubinstein, J. L., Barnhart, W. D., Earle, P. S., & Benz, H. M. (2017). Oklahoma experiences largest earthquake during ongoing regional wastewater injection hazard mitigation efforts. *Geophysical Research Letters*, 44, 711– 717. https://doi.org/10.1002/2016GL071685

Zecevic, M., De Barros, L., Eyre, T. S., Lokmer, I., & Bean, C. J. (2016). Relocation of long period (LP) seismic events reveals en echelon fractures in the upper edifice of Turrialba volcano, Costa Rica. *Geophysical Research Letters*, 43, 10,105– 10,114. https://doi.org/10.1002/2016GL070427

Zoback, M. D., Kohli, A., Das, I., & Mcclure, M. W. (2012). The importance of slow slip on faults during hydraulic fracturing stimulation of shale gas reservoirs. *Society of Petroleum Engineers*. https://doi.org/10.2118/155476-MS